

Computer-Assisted Microscopy

Fatima A. Merchant and

Kenneth R. Castleman

*Advanced Digital
Imaging Research*

1	Introduction.....	1311
2	Computer-Assisted Microscopy Systems	1312
2.1	Hardware • 2.2 Imaging Software	
3	Software for Hardware Control.....	1316
3.1	Automated Slide Scanning • 3.2 Autofocusing • 3.3 Image Capture	
4	Image Processing and Analysis Software	1318
4.1	Background Subtraction • 4.2 Color Compensation • 4.3 Segmentation for Object Identification • 4.4 The User Interface	
5	The Advanced Digital Imaging Research Computerized Microscopy System.....	1322
5.1	Hardware • 5.2 Software	
6	Applications in Clinical Cytogenetics	1323
6.1	Fetal Cell Screening in Maternal Blood • 6.2 Subtelomeric Fluorescent In Situ Hybridization for Detection of Cryptic Translocations • 6.3 Detection of Gene Duplications • 6.4 Four-Color Fluorescent In Situ Hybridization for Aneuploidy Screening • 6.5 Thick-Specimen Imaging • 6.6 Commercially Available Systems	
7	Conclusions.....	1338
	Acknowledgments	1338
	References	1338

1 Introduction

Recent advances in the field of microscopy have been driven not only by technologic innovations in engineering, optics, computer science, and precision manufacturing, but also by fundamental discoveries in chemical and biologic sciences. The last two decades have seen various changes to the microscope, resulting in the current modern microscope, which is a powerful tool in biologic research and development. Although most of the changes pertain to advances in optics, today's microscopes are also fitted with ergonomic features, and they include automation of several manual functions. Microscopes today offer automated focusing, selection of objectives and filters, light control, and a wide range of other features. Moreover, the increasing complexity of biologic experiments performed with optical microscopy, and the complexity of data that can be obtained, have resulted in even more sophisticated optical microscopy systems [1–5]. Although a completely automated microscope is not required in most applications, there are a growing number of applications,

such as screening a large number of specimens with different protocols, deconvolution, fluorescence resonance energy transfer (FRET) imaging, multispectral imaging and ion ratio imaging that require automated microscopes [6]. Furthermore, computer technology is changing the ways we access equipment, view samples, record, manage, and disseminate images. Digital imaging has created the need for archiving, managing, manipulating, and quantifying images. The coupling of computers to microscope systems has resulted in the development of optical imaging systems that can perform complicated experiments and provide more data, convenient storage of and access to the data, and, perhaps most important, substantial aid in the analysis of large volumes of data.

Quantitative methods for computer-assisted morphometry and cytometry have become well established during the past decade [7–9]. In complex experiments involving a myriad of peripheral devices, computer technology is useful for controlling filter wheels, shutters, automated stages, and cameras. Computer-assisted microscopy allows the extraction of quantitative, reproducible, diagnostically relevant information

while reducing subjective influences of human operators. It increases the quality and relevance of data and enables comparison and verification of the results. Standardized and automated systems are needed to generate consistent results among different experiments and laboratories while enhancing productivity and realizing cost savings. The advantages of computerized microscopy include the ability to (a) control and synchronize the functions of multiple peripheral devices, (b) extract information using quantitative methods, (c) analyze data to determine statistical significance, (d) reduce cost by relieving humans of tedious duties, and (e) support significantly expanded testing volumes without concomitant requirements for additional personnel and floor space.

Computerized microscopy is useful in (a) color and monochrome bright-field applications with thick specimens that require multiple optical sections (i.e., z-planes), (b) applications in fluorescence microscopy that require the acquisition of more than one wavelength, (c) applications that require large specimens to be scanned, (i.e., when adjacent areas need be scanned and “tiled” together to create a much larger image), and (d) time-lapse or motion analysis applications. Although computerized microscopy systems expedite data collection by automating the process, the real power of the system is the extraction from the images of useful, quantitative information that previously required human interpretation.

Generic digital image processing algorithms can often be applied successfully, but they sometimes fail to exploit fully the information contained in microscope images. This is because the optics that produced a particular image are poorly understood. Computerized microscopy systems need to tailor image-processing algorithms to particular forms of microscopy such as bright-field, dark-field, phase contrast, interference contrast, fluorescence, and confocal systems [10]. Further, the theory of microscopy is complicated, and agreement with data is less than perfect. The challenge is to synthesize theoretical models and empirical evidence in order to tackle particular image analysis problems [11].

Automated image analysis system design begins by specifying requirements for the system and then selecting image-processing functions that meet those requirements. It is difficult to describe a generic set of algorithms for object identification and classification, and actual systems are often limited to one or a few specific applications. Universal systems, capable of automatically learning and finding desired user information, do not exist.

In this chapter, we present an overview of what constitutes a microscope imaging system, with special emphasis on automation of image acquisition and analysis, and imaging techniques used in the context of biologic applications—specifically clinical cytogenetics. We describe an automated imaging system for use in clinical cytogenetics. Image analysis algorithms specific to particular applications are discussed separately. Instrumentation is discussed, including motorized

stages and filters, cameras and digitizer boards, and software algorithms including image enhancement, autofocusing, object detection and relocation, and features for operator review and data analysis for computerized microscopy.

2 Computer-Assisted Microscopy Systems

The modern microscopy imaging system is composed of five basic components: the microscope, a lighting source, a specimen stage control, an image acquisition device, and a postacquisition image analysis system. The microscope can be practically any high-end optical device, such as those offered by Leica, Meiji, Nikon, Olympus, and Zeiss, and one that meets the initial resolution and functionality requirements of the experiments for which the instrument will be used. The components of a computer-assisted microscopy system are depicted in Fig. 1. The core of any computer-assisted microscopy system is the microscope, which creates an image of the specimen. An image sensor, such as a charge-coupled device (CCD) camera or a photomultiplier tube (PMT), converts the magnified image to an analog voltage signal. The signal is then digitized and stored in a computer for later retrieval or analysis. Several peripheral devices, such as motorized X, Y stages, Z-axis motors, and filter wheels, are fitted to the microscope to perform different kinds of experiments. A host computer interfaces the separate hardware components to the microscope. Communication with the peripheral devices is through hardware boards that reside in the system's host computer and use the computer's internal bus. The PCI bus is well suited for imaging applications due to its high speed of operation and support from many manufacturers. Other types of connections include serial lines (RS-232, RS-485), USB, and the General Purpose Interface Bus (GPIB).

Automation is implemented via software tailored to control the experiment, for example by automatically selecting the wavelength and intensity of excitation light, positioning the specimen in the field of view (FOV), autofocusing, and capturing single- or multichannel images. The microscope and

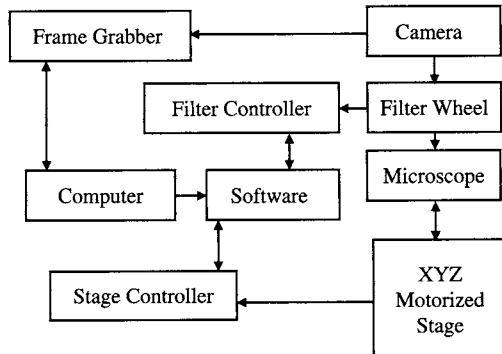


FIGURE 1 Components of a computer-assisted microscopy system.

the associated optics and detectors determine the quality of the image data obtained, and care must be taken to match the components to obtain the best possible results. Overall, the system contains computer software and hardware that can automatically scan microscope slides, find the optimal focus position, capture images, manipulate those images via pre-processing to remove noise, segment the images to identify objects therein, extract relevant information about each object (e.g., size, presence or absence of a diagnostic marker), and finally classify them according to the experimental specifications.

2.1 Hardware

The basic components of a computerized microscopy system can be broken down into three fundamental areas. These are (a) automation of the microscope's X, Y, and Z axes; (b) control of fluorescence excitation or bright-field illumination; and (c) control of the image sensing device. In most instances, these components can be added easily to any commercially available microscope. Motorized stages and filter wheels are readily available and can be custom fitted to a variety of different microscopes. Similarly, focus drives are available to control the Z-axis position of the stage (or the microscope head in the case of fixed stage microscopes). Automated X, Y stages allow movement of the stage in the X and Y axes, shutters control the exposure of both the fluorescent and incandescent light, monochromators or filter wheels are used to select a specific excitation wavelength, and image sensors, such as CCD cameras or PMT, capture images. Given the number of hardware options available, the selection of components depends on the efficiency and precision requirements of the particular application. Cortese [12] presents a listing of commercial vendors for a variety of microscope components.

2.1.1 Illumination Source

Most commercially available microscopes have built-in light sources for bright-field and fluorescence microscopy. For transmitted light microscopy, an incandescent tungsten-halogen bulb supplies illumination. Fluorescence microscopy, uses either mercury or xenon arc lamps. Most recently, EFOS Inc. (Mississauga, Ontario), has developed a novel fluorescence illuminator, the X-Cite®, which delivers a uniform FOV and maximum energy spectrum from a 50-W metal-halide lamp, outperforming 100-W mercury-arc lamps with a 2,000-hour lifespan. Alternatively, Photon Technology International Inc. (Lawrenceville, NJ) has developed the NovaLight™, an illuminator that delivers up to seven times the output of conventional arc lamps.

In fluorescence illumination, the excitation light and emission light are controlled by filters inserted in the light path between the illuminator and the specimen, and again between the specimen and the image sensor. A wide variety

of filter cubes is available from major manufacturers, who produce filter sets suitable for most of the common fluorophores in use today. Other illumination sources include arc-discharge lamps and light-emitting diodes (LEDs). Lasers can also be used as light sources, but they are expensive and are commonly employed for specialized techniques such as confocal fluorescence microscopy, optical trapping, and lifetime imaging studies, photobleaching recovery studies, and total internal reflection fluorescence imaging.

Mechanical or electronic optical shutters can be used to control the amount of time that the specimen is exposed to illumination. They typically allow various opening and closing patterns and can allow 100% transmission or complete extinction of the light. The minimum opening speed of most commercially available shutters is on the order of 10 milliseconds. In multimode light microscopy applications, they are often used to switch between transmitted and fluorescence imaging, with shutters in both the transmitted light path and the fluorescence path. Shutters come with computer interface controllers that allow both manual and remote opening and closing. Controlling the exposure time can reduce photobleaching in fluorescence imaging applications.

2.1.2 Filter Control

Filter wheels are used on microscopes, cameras, and video systems to position a selected filter in the imaging path quickly and accurately. Typically, a filter, or combination of filters, is used to attenuate the light intensity, or to prevent unwanted spectral wavelengths from contaminating the recorded image. They are used in machine vision, parts inspection, and research applications, especially those involving fluorescent microscopy, spectrophotometry, photometry, color photography, and optical and infrared imaging.

Fluorescence illumination and observation is the most rapidly expanding microscopy technique employed today in the medical and biologic sciences. Fluorescence probes (fluorochromes) have unique individual excitation and emission spectra. Typically, there is overlap between the higher wavelength end of the excitation spectrum and the lower wavelength end of the emission spectrum. A combination of filters (made up of an excitation filter, a dichromatic beamsplitter, and a barrier filter) is used to separate the excitation and emission light and improve image contrast. This is achieved by the proper selection of filters to block or pass specific wavelength bands of the spectrum. Chroma Technology Corp. (Brattleboro, VT) and Omega Optical Inc. (Brattleboro, VT) provide a number of filter sets designed for specific combinations of fluorescence probes for a variety of single- and multiple-labeling fluorescence microscopy applications.

In automated microscopy, a convenient approach to providing the required wavelengths of excitation light is

to use a filter wheel coupled with a multispectral lamp (e.g., mercury, or xenon). Filter wheels can be fitted to either the excitation or emission (or both) ports of a microscope. Mounting flanges allow filter wheels to be effectively inserted into the optical path of most microscopes without affecting camera or eyepiece focus. In epifluorescence microscopy, excitation filter wheels control the illumination spectrum before it enters the objective, whereas emission filter wheels are mounted on the camera port and select a unique emission wavelength.

Another common application of a filter wheel is to introduce neutral density (ND) filters into the optical path. ND filters attenuate the light passing through the microscope optics. This can allow the lamp to operate at a higher brightness level (to provide enhanced color balance) and they afford aperture adjustment for depth-of-field effects without saturating the camera. Typically, ND filters are graduated in degrees of light absorption.

Filter wheels are generally available with mountings for between three and twelve filters. The filters in the wheel may be of different colors, thickness, or materials. For multispectral applications requiring a large number of wavelengths, two or more filter wheels may be used, to allow for more filters, or to control separately the upper and lower cutoff wavelengths of a passband. For example, a dual-filter wheel system with two six-filter wheels could provide ten individual filters (one open position in each wheel), with the potential for as many as 36 combinations. The most common use of dual-filter wheels is to combine a bandpass filter with an ND filter to control the wavelength and intensity of the fluorescence excitation.

For automated microscopy applications, motorized filter wheels with controller systems are interfaced to a computer, permitting direct communications via RS-232, GPIB, or USB serial ports. Typically, such systems also offer optional filter wheel control via a keypad. Automation and programming of unique filter sequences are conducted through the RS-232 interface. A simple command language (provided by the manufacturer) is used to retrieve filter status and to select filters. Often, an integrated shutter can be opened and closed by commands sent to the serial port. The typically adjacent filter switching speed of commercially available shutters is on the order of 30 to 100 milliseconds. Filter wheel are provided by vendors such as Prior Scientific, Inc. (Rockland, MA), Ludl Electronic Products, Ltd. (Hawthorne, NY), Applied Scientific Instruments (Eugene, OR), and Marzhauser Wetzlar (Wetzlar-Steindorf, Germany).

2.1.3 X, Y Stage Positioning and Z-Axis Motors

X, Y motorized stages and Z-axis (focus drive) motors form an integral part of any computer-assisted microscopy system. They allow a specimen to be positioned accurately and automatically relative to the microscope objective. They also allow optical sectioning of thick specimens and automatic

focus. The stages can be customized to hold specimens on microscope slides, Petri dishes, or cell plates. X, Y linear translation stages are typically driven by a stepper motor and a controller that interfaces to the host computer. Typically, the X, Y resolution of such systems is ranges from 0.1 to 5 μm .

Translation stages are important because they allow automated scanning of specimen slides, thus increasing the speed of data collection. An important feature of computer controlled motorized stages, is the ability to move the slide to a previously located position. This is useful in experiments where serial observations of a specimen require removal, restaining, and subsequent return of specimens to the microscope stage. Specimen positioning provides the ability to return to specific coordinates, and thus to view the same region of the slide that was observed prior to removal of the slide.

Z-axis motors allow controlled movement of the specimen in the vertical (Z or axial) direction, thus providing the capability for automatic focusing, and collection of optical sections of specimens (i.e., sets of images taken at different focal planes). The minimum Z-axis step size of typical focus motors can range from 0.01 to 0.05 μm .

Burleigh Instruments Inc. (Fishers, NY), offers an extensive line of micropositioning devices for the life sciences. Prior Scientific Inc. (Rockland, MA), has the OptiScanTM and ProScanTM stage products that fit most upright and inverted microscopes and include a controller capable of managing the stage. Other vendors include Ludl Electronic Products, Ltd. (Hawthorne, NY), Applied Scientific Instruments (Eugene, OR), Sutter Instrument Company (Novato, CA), and Marzhauser Wetzlar (Germany).

2.1.4 Image Sensors

With the advent of high-resolution solid-state cameras, such as the slow scan, cooled CCD camera, photographic film cameras are now being replaced by digital imaging systems. CCDs are the most frequently used image detectors as they have many advantages including larger dynamic range, good quantum efficiency, low noise, linear response, and negligible geometric distortion. CCD cameras are extensively used because of their low-light-image capturing ability. A CCD camera is a light-sensitive, silicon, solid-state device. This imaging technology is based on collecting photons on the surface of a silicon grid containing many collection wells or pixels (for example, a 512×512 -pixel grid). The photons within a well are subsequently converted to an electrical charge via the photoelectric effect, which is then passed to an image digitizer for conversion into an electrical signal that represents the intensity of the pixel. The intensities for all pixels over the grid are organized as a digital image and projected as a single video frame.

The variety of light detection methods and the number of imaging devices currently available [12] to the researcher

make the selection process complex and often confusing. Many types of image sensors exist, and the choice is often dictated by the requirements of a given experiment. CCD camera selection typically involves the choice of appropriate parameters for several features. Two operational modes interlaced scan and progressive scan are available. Interlaced cameras scan an image in two steps, usually odd and even horizontal lines, and then reconstruct it in a buffer, which decreases monitor flickering. Progressive-scan cameras transfer an entire image without interlacing. Another design issue in CCD cameras is the number of chips. Single-chip cameras generate color using specialized sensor areas that detect R (red), G (green), and B (blue) components, whereas multiple-chip designs (3CCD) use a beam-splitter and R-, G-, and B-chips to detect each color component. The resolution is higher for the 3CCD cameras when compared with single-chip cameras. The sensor size of the camera determines its sensitivity and resolution. CCD cameras also have a frame rate of more than 30 frames per second and a digital output rate (usually in cycles/second or hertz) dependent on the analog—digital converter. CCD cameras can be “cooled” to subzero temperatures, thus minimizing noise and thermal variations, which reduces the dark current (i.e., the charge accumulated within the CCD, in the absence of light) and allows longer integration times for image capture. The digital dynamic range or bit depth is another important feature when choosing a CCD camera. For example, an 8-bit image can store 256 shades of gray and a 12-bit image can store 4,096. A 12-bit image can reveal greater detail than an 8-bit one; and quantification is more precise in 12-bit images. The level of overall noise (in decibels, or dB) for a CCD camera, is usually expressed as a signal/noise (S/N) ratio: $S/N (dB) = 20^* \log (S/N)$. Thus, an S/N ratio of 100/1 is equivalent to 40 dB. Due to the low-light conditions inherent in fluorescence imaging, camera sensitivity is more critical here than in transmitted light microscopy. To increase sensitivity for low-light observation, image intensifiers may be used to amplify light before it reaches the camera faceplate. CCDs that are not intensified may increase sensitivity using “binning” (or “superpixeling”). This technique increases sensitivity and frame rate by grouping pixel intensities.

Specialty cameras are particularly well suited for scientific applications in computerized microscopy systems since they offer unique features like large chip area, resolution up to 4000×4000 k pixels, digital output, cooling to reduce noise and dark current, flexible timing, and full computer control. Suppliers of CCD cameras include Cooke Corporation (Auburn Hills, MI), Diagnostic Instruments (Sterling Heights, MI), Dage-MTI Inc. (Michigan City, IN), Optronics Inc. (Muskogee, OK), Cohu Inc. (San Diego, CA), and Roper Scientific Inc. (Duluth, GA). Cortese [12] provides a comprehensive listing of camera vendors.

Frame grabbers are image processing computer boards that capture and store image data. In a computerized microscopy

system, digitizer boards (frame grabbers) are typically used in conjunction with CCD cameras for digitizing the microscope image for further analysis and permanent storage. The type of imaging board must be matched to the camera in terms of type of signal format, resolution, and precision. Acquisition formats include RS170, CCIR, RS330, RS422, NTSC, Y/C, PAL, and RGB. For frame grabbers that can handle camera outputs in digital format the input pixel acquisition depth is important to consider. The pixel depth refers to the number of bits used to store the gray level at each pixel. Increasing pixel depth increases the amount of detail that can be reproduced in the scanned image. Frame grabbers are available in 8-, 12-, 16-, and 24-bit pixel depth formats. The 8-, 12-, and 16-bit frame grabbers allow digitization of monochrome images, whereas 24-bit frame grabbers are designed to work with RGB cameras can be used to acquire three monochrome video signals synchronously. Frame grabbers are provided by Scion Corporation (Frederick, MD), MuTech Corporation (Billerica, MA), and National Instruments (Austin, TX).

2.2 Imaging Software

In computerized microscopy systems, the complexity and number of variables that need to be configured, monitored, and adjusted prior to and during data collection are enormous, but they can easily be managed by software created specifically for this purpose. For example, to create a three-dimensional (3D) image of a thick specimen, images of the sample are taken as the specimen stage is systematically and carefully moved along the z-axis. For multiple fluorescent probe analyses on the same sample, the change in excitation wavelength and collection of emission data must be precisely controlled. These and other experimental operations are controlled and managed by the software. Software plays a major role in computer-assisted microscopy.

The software of an automated microscopy system has three functions: (a) control of peripheral devices (stage, filter, camera, etc.), (b) image processing and analysis, and (c) the user interface. Peripheral devices are controlled by integrated computer interfaces (controllers) or proprietary interface cards. This component includes the core functions of the automated imaging system. It involves the control of the motorized stage for slide scanning, the focus motor for autofocusing and optical sectioning, the filter wheel control for filter selection, shutter control, and camera integration time, and image capture and storage.

The second software component involves image preprocessing and analysis. Typical algorithms integrated in this component include image editing functions, geometric manipulations, morphologic filtering, smoothing, background subtraction, color separation, object segmentation, and classification. This software component is also responsible for collecting and storing additional information about the experiment, such as excitation wavelength; number of frames

averaged, time, date, and other information pertinent to the experiment.

The user interface component is critical for user control and communicating with the other components of the software package, as well as providing feedback and reporting results. Commonly used graphic user interface (GUI) elements include (a) buttons for simple actions such as grabbing an image, (b) input fields for numeric values and textual information, (c) menus for choices, (d) windows for displaying acquired images, and (e) windows presenting extracted information about the current experiment.

3 Software for Hardware Control

Devices such as cameras, filter wheels, and microscope stages can be controlled by commands sent through an RS-232 serial connection. Typically, the device will respond with confirmations or status information. Every device uses a particular communication protocol and has its own set of commands. Software designed to integrate such equipment needs to send the appropriate commands and act on any information that comes back from the device. Typical operations include transmitting and receiving serial data, correctly terminating commands, recognizing incoming commands, flushing the serial buffers, and waiting while a device is busy. Stage controllers, for example, move samples under a microscope in one or more axes. The commands sent to an axis motor typically include operations such as the following: Home (move the stage to the home position in this axis), Move (move to an absolute position), and, Relative move (move to a position relative to the current position). These commands are defined by the manufacturer of the device and can be easily integrated into the algorithms that interact with the peripheral devices. Some of the key algorithms used in computerized microscopy are described in the following sections.

3.1 Automated Slide Scanning

Scanning a specimen slide involves repeating a series of steps until the entire slide, or a user-defined area thereof, has been scanned. In a typical scanning algorithm, each FOV is focused automatically, after which an image is acquired. When image capture is complete, the stage is moved to the next FOV. Generally, an algorithm to implement automated slide scanning moves the slide in a raster pattern. For example, it moves vertically down the user-selected area and then retraces back to the top, moves a predetermined fixed distance across and then starts another scan vertically downward. This process is continued until the entire user-defined area has been scanned. The step sizes in the X and Y directions are adjusted (depending on the pixel size for the objective in use) so that there is no overlap between the adjacent fields.

Scanning speed is an important feature in a computerized microscopy system. Factors that influence the scanning rate

include stage movement, filter movement, the readout rate of the CCD chip, and the time required for focusing. The scanning rate is computed as the total area scanned per unit time. It also depends upon the sampling density of the image, varying inversely with the square of the sampling density and the integration time [10].

The cutoff frequency ϖ_c for an imaging system is given by

$$\varpi_c = \frac{4\pi \cdot NA}{\lambda} \quad (1)$$

where NA is the numeric aperture, and λ is the wavelength.

The Nyquist sampling theorem states that an image can be reconstructed from its samples without error if the sampling frequency is at least $2 \cdot \varpi_c$. Sampling density is defined as the number of pixels per unit length. The choice of sampling density can be based on the Nyquist sampling theorem or on the required measurement precision. The decision should be based on the requirements of the system. For autofocusing, depth-of-focus, or image restoration applications, the Nyquist theorem should be used. If measurements derived from microscope images are required, then the sampling frequency should be derived from the measurement specifications [11].

3.2 Autofocusing

Automatic focusing is essential for automated microscopy when fully automated image acquisition in unattended operation is required. It also facilitates objective and consistent image measurements for quantitative analysis.

Two approaches are used for autofocusing. One, known as “active” focusing, is based on surface sensing, whereas the other, known as “passive” focusing, is based on image analysis. Surface sensing methods require a single surface from which light or sound is reflected, and calibration of the in-focus location. These methods are generally impractical for light microscopy since there is usually more than one reflective surface (e.g., slide and coverslip), and specimens vary in thickness. The image analysis approach depends only on focus measurements from the image itself. The in-focus position is found by locating the maximum of a focus function computed on a series of images acquired at different Z-axis positions. The focus function is a measure of image sharpness, as a function of Z-axis position. A sequence of images taken along the Z-axis has to be acquired to find the focus position. The value of the focus function is computed for each image captured at a different z-position. The maximum value of the focus function identifies the optimal focal plane. These methods are not sensitive to multiple reflective surfaces and therefore are widely used in light microscopy.

3.2.1 Focus Functions

Several groups have developed and tested focus functions for automated microscopy. Johnson and Goforth at Jet Propulsion Laboratory (JPL) [13] and Dew et al. [14] used

hardware that integrates the high-pass filtered video signal in a real-time autofocusing system. Harms and Aus [15] evaluated a Laplacian-based autofocus parameter that mimics the receptive fields in the human eye. Groen et al. [16] advanced eight criteria for evaluating autofocus parameters and compared 11 parameters. Their results varied somewhat with different types of specimens, but two “gradient squared” functions, along with gray-level variance, proved best in their testing on bright-field images. Boddeke et al. [17] argued that the most effective autofocus parameters emphasize the mid-frequency range, since the OTF does not change with defocus at either the high- or low-frequency end. They also argued for binning to reduce noise and for fitting a parabola to the focus parameter values to interpolate the exact point of best focus. Firestone et al. [18] tested autofocus functions and found those that summed gradients were effective. Vollath presented new autofocus functions based on autocorrelation [19] and considered the effects of noise [20]. Brenner et al. [21], Erteza [22, 23], and Muller and Buffington [24] also advanced and tested autofocus functions based on the sum of squared gradients. Price and Gough [25] advanced a new prefiltered two-dimensional (2D) Laplacian parameter and evaluated eleven functions in fluorescence and phase-contrast microscopy. They found that, in fluorescence microscopy (a) the gradient-based parameters gave sharper peaks, and thus had narrower operating ranges than the statistical parameters; (b) the gradient and statistical techniques did not agree exactly on the point of best focus; and (c) autocorrelation-based parameters performed similarly to gradient-based ones. Geusebroek et al. [26] proposed an autofocusing algorithm based on the signal power after convolving the image with a first-order derivative of a Gaussian filter. This technique was found to be generally applicable to several light microscopy modalities including fluorescence, bright field, and phase-contrast microscopy, on a wide variety of preparation and specimen types. An exhaustive search for finding the maximum focus position was used to circumvent problems caused by noisy focus function curves. Santos et al. [27] systematically evaluated 13 autofocus functions for analytic fluorescent image cytometry studies of counterstained nuclei. Using a proposed figure-of-merit criterion that weighs five different features of a focus function, the test results suggested that focus functions based on correlation measures had the best performance for the type of images they studied. Selecting an appropriate focus function is critical for autofocusing, and it depends largely on the requirements of the system, specifically the mode of microscopy and the type of specimens being examined.

The step size for obtaining a sequence of images along the z-axis can be computed using the focal depth of a microscope objective, which is approximately

$$\text{DOF} = \frac{\lambda}{2 \cdot NA^2} \quad (2)$$

where λ is the wavelength, and NA is the numeric aperture of the objective.

One can take a series of images spaced by approximately that distance along the optical axis of the microscope to effect the optical equivalent of serial sectioning.

3.2.2 Autofocus Speed

An important factor in most autofocusing is the time-consuming nature of the procedure. To reduce autofocusing time when scanning a slide, the number of FOVs that are focused should be reduced. This may be achieved by extrapolation or interpolation strategies to estimate the focus position of most fields based on the measured focus positions of a few fields. Interpolation can be used to estimate the focus position of a particular field from previously measured positions from at least three adjacent fields. This estimation is thus based on local information, and a focusing error in one field will only influence the estimated focus position of neighboring FOVs. In the interpolation approach, the focus positions of a number of FOVs across the entire slide have to be measured initially. A linear surface ($z = ax + by + e$) is then fitted through these measured values. During scanning, the fitted linear surface is used to calculate the focus position of each field. A disadvantage of this approach arises when the area to be scanned is large. For increased scanning times, the linear fit is may not reliable because the position of the focal plane may change over time due to temperature-induced sample variations.

Another approach to improve the speed of autofocusing algorithms is to use a two-phase focusing approach. Initially, a coarse focus phase may be implemented using larger z-step sizes. The first two samples are used to determine the direction of the focus. The algorithm then steps in the determined direction until the last focus value is lower than the previous one. The in-focus z-position is then located between adjacent z-positions with the highest and second highest focus value. A second, fine-focus phase then repeats the same procedure with smaller z-step sizes. The starting point is the optimal focus position determined by the coarse focus phase. The fine-focus phase then samples the focus function along N positions equidistant about the coarse phase in-focus z-position. The final estimation of the in-focus z-position is calculated through a quadratic fit of the N points. The outcome of a robust autofocus algorithm should be a sharp peak in the focus function at the in-focus position as shown in Fig. 2. The selected autofocus algorithm for computerized microscopy should be generally applicable on a large variety of microscopic modes, and a large variety of preparation techniques and specimen types.

3.3 Image Capture

Most frame grabber boards come with source code examples designed to illustrate important features of the board.

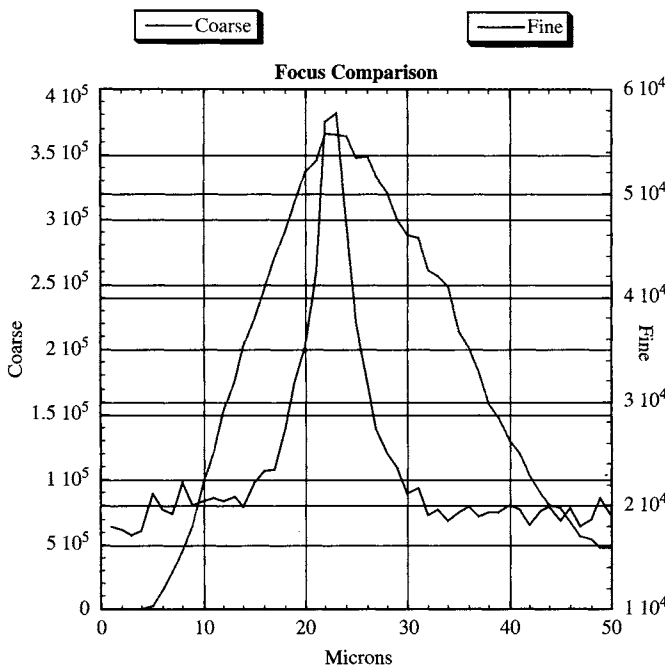


FIGURE 2 Two-phase approach to autofocusing, using a coarse focus and a separate fine focus function (see color insert).

The features covered include initialization, triggering, and real-time control of Input/Output (I/O) lines. Customized software for image capture can be developed around the drivers and libraries provided by the manufacturers of the camera and digitizer boards.

4 Image Processing and Analysis Software

In any computerized microscopy system, quantitative data are obtained, and certain tasks are automated, using image processing and analysis techniques. Most automated microscopy applications are based on the measurement of features that cannot be obtained reliably by visual inspection. While visualization of images allows a qualitative analysis of the objects of interest, quantitative measures are usually essential to define and understand the biologic processes. Digital image processing theory provides a number of tools to enhance images and to measure size, shape, and intensity features accurately. In addition to autofocusing, scanning, and image capture algorithms, computerized microscopy requires specific image processing algorithms to obtain the desired results. We discuss some of those here.

4.1 Background Subtraction

Quantitative image analysis typically involves measuring the brightness of regions in the image as a means of identification, that is it is often assumed that the same type of feature will

be similar in intensity wherever it appears in the image. Differences in intensity values among different object features can then be used to differentiate between several features for counting, measurement, or identification. In most imaging processes, illumination sources can create intensity variations across the FOV. Even with proper calibration, one can only approximate uniform illumination of the scene being imaged. This is particularly true for a microscope system. Both the halogen (transmitted light) and mercury (fluorescent light) lamps have to be adjusted for uniform illumination of the FOV prior to use. Moreover, microscope optics and/or cameras may also show vignetting, in which the corners of the image are darker than the center because the light is partially absorbed. The process of eliminating these defects by application of image processing to facilitate object segmentation, or to obtain accurate quantitative measurements is known as background correction or background flattening.

4.1.1 Background Subtraction

For microscopy applications, two approaches are popular for background flattening [28]. In the first approach, a “background” image is acquired in which a uniform reference surface or specimen is inserted in place of actual samples to be viewed, and an image of the FOV is recorded. This is the background image, and it represents the intensity variations that occur without a specimen in the light path, only due to any inhomogeneity in illumination source, the system optics, or camera, and can then be used to correct all subsequent images. When the background image is subtracted from a given image, areas that are similar to the background will be replaced with values close to the mean background intensity. The process is called background subtraction and is applied to flatten or even out the background intensity variations in a microscope image. It should be noted that, if the camera is logarithmic with a gamma of 1.0, then the background image should be subtracted. However, if the camera is linear, then the acquired image should be divided by the background image. Background subtraction can be used to produce a flat background, and compensate for nonuniform lighting, non-uniform camera response, or minor optic artifacts (such as dust specks that mar the background of images captured from a microscope). In the process of subtracting (or dividing) one image by another, some of the dynamic range of the original data will be lost.

4.1.2 Surface Fitting

The second approach is to use the process of surface fitting to estimate the background image. This approach is especially useful, when a reference specimen or the imaging system is not available to experimentally acquire a background image [29]. Typically, a polynomial function can be used to estimate variations of background brightness as a function of location. The process involves an initial determination of an

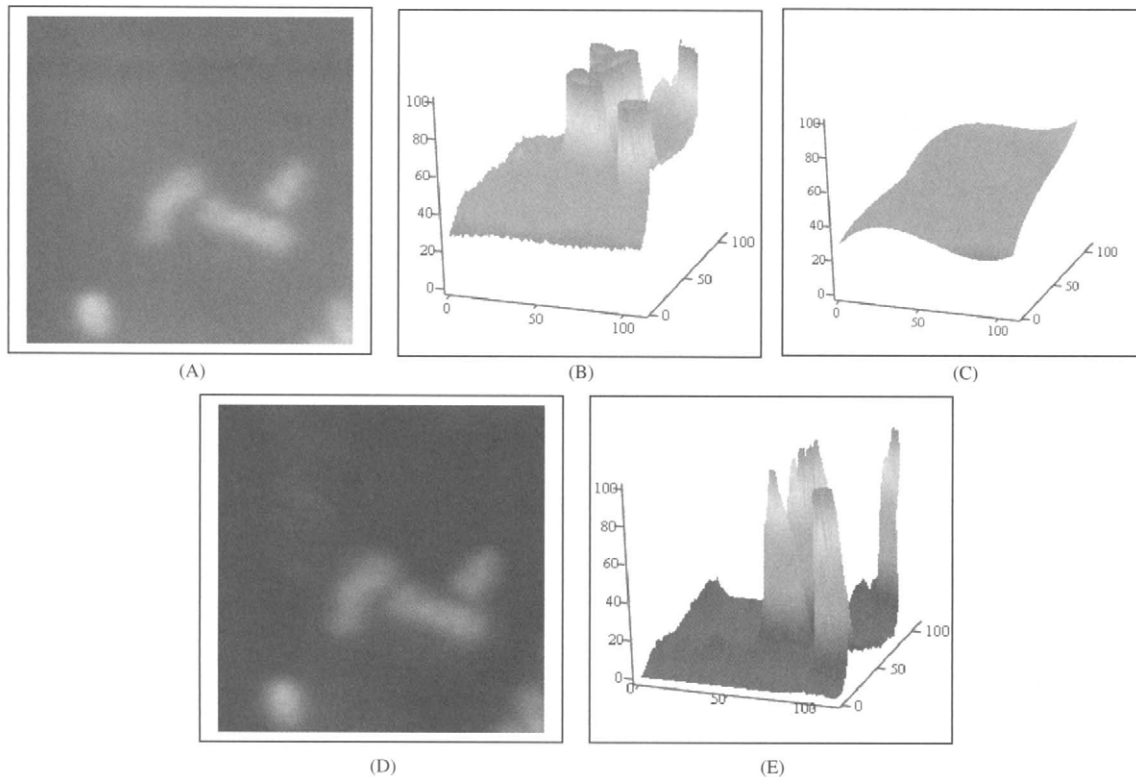


FIGURE 3 (A–E): Background subtraction via surface fitting. Panel A shows the original image, panel B presents its 2D intensity distribution as a surface plot, panel C shows the background surface estimated via the surface fitting algorithm, panel D shows the background subtracted image, and panel E presents its 2D intensity distribution as a surface plot.

appropriate grid of background sampling points. By selecting a number of points in the image, a list of brightness values and locations can be acquired. In particular, it is critical that the points selected for surface fitting represent true background areas in the image, and not foreground (or object) pixels. If a foreground pixel is mistaken for a background pixel, the surface fit will be biased, resulting in an over estimation of the background. In some cases, it is practical to locate the points automatically for background fitting. This is feasible when working with images, which have distinct objects that are well distributed throughout the image area and contain the darkest (or lightest) pixels present. The image can then be subdivided into a grid of smaller squares or rectangles, the darkest (or lightest) pixels in each subregion, and these points used for the fitting [29]. Another issue is the spatial distribution and frequency of the sampled points. The greater the number of valid points that are uniformly spread over the entire image, the greater the accuracy of the estimated surface fit. A least-squares fitting approach may then be used to determine the coefficients of the polynomial function. For a third-order polynomial, the functional form of the fitted background is:

$$\begin{aligned} B(x, y) = & a_0 + a_1 \cdot x + a_2 \cdot y + a_3 \cdot xy + a_4 \cdot x^2 + a_5 \cdot y^2 \\ & + a_6 \cdot x^2y + a_7 \cdot xy^2 + a_8 \cdot x^3 + a_9 \cdot y^3 \end{aligned} \quad (3)$$

This polynomial has 10 ($a_0 - a_9$) fitted constants. To get a good fit and diminish sensitivity to minor fluctuations in individual pixels, it is usual to require several times the minimum number of points. We have found that the minimum number of points is approximately about three times the total number of coefficients to be estimated. Figure 3A–E demonstrates the process of background subtraction. Panel A shows the original image, panel B presents its 2D intensity distribution as a surface plot, panel C shows the background surface estimated via the surface fitting algorithm, panel D shows the background-subtracted image, and panel E presents its 2D intensity distribution as a surface plot.

4.1.3 Other Approaches

Another approach used to remove the background is frequency domain filtering. It assumes that the background variation in the image is a low-frequency signal, and can be separated in frequency space from the higher frequencies that define the foreground objects in the image. A high-pass filter can then be used to remove the low-frequency background components [28].

Other techniques for removing the background include nonlinear filtering [30] and mathematic morphology [31].

Morphologic filtering is used when the background variation is irregular and cannot be estimated by surface fitting. The assumption behind this method is that foreground objects are limited in size and smaller than the scale of background variations, and the intensity of the background differs from that of the features. The approach is to use an appropriate structuring element to describe the foreground objects. Neighborhood operations are used to compare each pixel with its neighbors. Regions larger than the structuring element are taken as background. This operation is performed for each pixel in the image, and a new image is produced as a result. The result of applying this operation to the entire image is to shrink the foreground objects by the radius of the structuring element, and to extend the local background brightness values into the area previously covered by objects.

Reducing brightness variations by subtracting a background image, whether it is obtained by measurement, mathematic fitting, or image processing, is not a cost-free process. Subtraction reduces the dynamic range of the gray scale, and clipping must be avoided in the subtraction process or it might interfere with subsequent analysis of the image.

4.2 Color Compensation

Many of the problems encountered in the automatic identification of objects in color (RGB) images result from the fact that all three fluorophores appear in all three color channels due to the unavoidable overlap among fluorophore emission spectra and camera sensitivity spectra. The result is that the red dye shows up in the green and blue channel images, and the green and blue dyes are smeared across all three color channels as well. Castleman [1994] describes a process that effectively isolates three fluorophores by separating them into three-color channels (RGB) of the digitized color image. The method, which can account for black level and unequal integration times [32], is a preprocessing technique that can be applied to color images prior to segmentation.

The technique yields separate, quantitative maps of the distribution of each fluorophore in the specimen. The premise is that the imaging process linearly distributes the light emitted from each fluorophore among the different color channels. For example, for an N -color system, each $N \times 1$ pixel vector needs to be premultiplied by an $N \times N$ compensation matrix. Then, for a three-color RGB system, the following linear transformation may be applied:

$$y = ECx + b \quad (4)$$

where y is the vector of RGB gray levels recorded at a given pixel and x is the 3×1 vector of actual fluorophore brightness at that pixel. C is the 3×3 color smear matrix, which specifies how the fluorophore brightnesses are spread among the three color channels. Each element c_{ij} is the proportion of the brightness from fluorophore i that appears in the color

channel j of the digitized image. The elements of this matrix are determined experimentally for a particular combination of camera, color filters, and fluorophores. E specifies the relative exposure time used in each channel, i.e., each element e_{ij} is the ratio of the current exposure time for color channel i , to the exposure time used for the color-spread calibration image. The column vector b accounts for the black-level offset of the digitizer, that is, b_i is the gray level that corresponds to zero brightness in channel i .

Then the true brightness values for each pixel can be determined by solving equation (4) as follows:

$$x = C^{-1}E^{-1}[y - b] \quad (5)$$

Where C^{-1} is the color compensation matrix. This model assumes that the gray level in each channel is proportional to integration time and the black levels are constant with integration time. With CCD cameras, both of these conditions are satisfied to a good approximation.

4.3 Segmentation for Object Identification

The ultimate goal of most computerized microscopy applications is to identify in images unique objects that are relevant to a specific application. Segmentation refers to the process of separating the desired object (or objects) of interest from the background in an image. A variety of techniques can be used to do this. They range from the simple (such as thresholding and masking) to the complex (such as edge/boundary detection, region growing and clustering algorithms). The literature contains hundreds of segmentation techniques, but there is no single method that can be considered good for all images, nor are all methods equally good for a particular type of image. Segmentation methods vary depending on the imaging modality, application domain, method being automatic or semi-automatic, and other specific factors. While some methods use pure intensity-based pattern recognition techniques such as thresholding followed by connected component analysis [33–34], other methods apply explicit models to extract information [35–37]. Depending on the image quality and the general image artifacts such as noise, some segmentation methods may require image preprocessing prior to the segmentation algorithm [38–39]. On the other hand, some methods apply postprocessing to overcome the problems arising from over segmentation.

4.3.1 The Segmentation Process

There are several approaches to segmentation such as (a) pattern recognition techniques [40], (b) model-based approaches [41], (c) tracking-based approaches [42], (d) artificial intelligence-based approaches [43], and (e) neural network-based approaches [44]. Pattern recognition techniques are further divided into four categories: (a) multiscale approaches, (b) region growing approaches, (c) differential

geometry-based approaches, and (d) mathematic morphology schemes. Morphologic approaches include techniques such as skeleton-based approaches, region-growing approaches, edge-based approaches, and matching filters approaches. Model-based approaches are further divided into two categories: deformable models and parametric models. Although there is a wide range of segmentation methods in different categories, sometimes multiple techniques are used together to solve different segmentation problems.

In most biomedical applications, segmentation is a two-class problem, namely the objects, such as cells, nuclei, chromosomes, and the background. Thresholding is a region-based approach that is useful for segmenting objects from a contrasting background. Thus, it is commonly used when segmenting microscope images of cells. Thresholding consists of segmenting an image into two regions: a particle region and a background region. In its most simple form, this process works by setting to white all pixels that belong to a gray-level interval, called the threshold interval, and setting all other pixels in the image to black. The resulting image is referred to as a binary image. For color images, three thresholds must be specified, one for each color component. Threshold values can be chosen manually or by using automated techniques. Automated thresholding techniques select a threshold, which optimizes a specified characteristic of the resulting images. These techniques include clustering, entropy, metric, moments, and interclass variance. Clustering is unique in that it is a multiclass thresholding method. In other words, instead of producing only binary images it can specify multiple threshold levels, which result in images with three or more gray-level values.

4.3.2 Threshold Selection

Threshold determination from the image histogram is probably one of the most widely used techniques. When the distributions of the background and the object pixels are known and unimodal, then the threshold value can be determined by applying the Bayes rule [45]. However, in most biologic applications, both the foreground object and the background distributions are unknown. Moreover, most images have a dominant background peak present. In these cases, two approaches are commonly used to determine the threshold. The first approach assumes that the background peak shows a normal distribution, and the threshold is determined as an offset based on the mean and the width of the background peak. The second approach, known as the triangle method, determines the largest vertical distance from a line drawn from the background peak to the highest occurring gray-level value [45].

Many thresholding algorithms are published in the literature, and selecting an appropriate one can be a difficult task. The selection of an appropriate algorithm depends upon the image content, and type of information required

postsegmentation. Some of the common thresholding algorithms are discussed. The Ridler and Calvard [46] algorithm uses an iterative clustering approach. The mean image intensity value is chosen as an initial estimate of the threshold is made. Pixels above and below the threshold are assigned to the object and background classes, respectively. The threshold is then iteratively estimated as the mean of the two class means. The Tsai [47] algorithm determines the threshold so that the first three moments of the input image are preserved in the output image. The Otsu [48] algorithm is based on discriminant analysis and uses the zero- and first-order cumulative moments of the histogram for calculating the threshold value. The image content is classified into foreground and background classes. The threshold value is the one that maximizes between-class variance, or equivalently minimizes within-class variance. The Kapur et al. [49] algorithm uses the entropy of the image. It also classifies the image content as two classes of events with each class characterized by a probability density function (pdf). The method then maximizes the sum of the entropy of the two pdf's to converge to a single threshold value.

Depending on the brightness values in the image, a global or adaptive approach for thresholding may be used. If the background gray level is constant throughout the image, and if the foreground objects have an equal contrast that is above the background, then a global threshold value can be used to segment the entire image. However, if the background gray level is not constant, and the contrast of objects varies within the image, then an adaptive thresholding approach should be used to determine the threshold value as a slowly varying function of the position in the image. In this approach, the image is divided into rectangular subimages, and the threshold for each subimage is determined [45].

4.4 The User Interface

The final component of the software package for a computerized microscopy system is the graphical user interface. The software for peripheral device control, image capture, preprocessing, and image analysis has to be embedded in a user interface. Dialogue boxes are provided to control the automated microscope, to adjust parameters for tuning the object finding algorithm, to define the features of interest, and to specify the scan area of the slide and/or the maximum number of objects that have to be analyzed. Parameters such as object size and cluster size are dependent on magnification, specimen type, and quality of the slides. These parameters can be tuned by the operator on a trial-and-error basis. Windows are available during screening to show the performance of the image analysis algorithms and the data generated. In addition, images containing relevant information for each scan must be stored in a gallery for future viewing, and for relocation if required. The operator can scroll through this window and rank the images according to the

features identified. This allows the operator to select for visual inspection those images containing critical biologic information.

5 The Advanced Digital Imaging Research Computerized Microscopy System

Our group has developed a computerized microscopy system for the use in the field of clinical cytogenetics.

5.1 Hardware

The instrument is assembled around a Zeiss Axioskop or an Olympus BX-51 epi-illumination microscope, equipped with a 100-W mercury lamp for fluorescence imaging and a 30-W halogen source for conventional light microscopy. The microscope is fitted with a ProScan motorized scanning stage system (Prior Scientific Inc. Rockland, MA), with three degrees of motion (X, Y, and Z), and a four-specimen slide holder. The system provides 9×3 -inch travel, repeatability to $\pm 1.0 \mu\text{m}$, and step size from 0.1 to $5.0 \mu\text{m}$. The translation and focus motor drives can be remotely controlled via custom computer algorithms, and a high-precision joystick is included for operator control. The spatial resolution of the scanning stage is $0.5 \mu\text{m}$ in X and Y and $0.05 \mu\text{m}$ in the Z-direction, allowing precise coarse and fine control of stage position. A Dage 330T cooled triple-chip color camera (Dage-MTI Inc. Michigan City, IN) capable of on-chip integration up to 8 seconds and 575-line resolution, is used with a Scion-CG7 (Scion Corporation, Frederick, ML) 24-bit frame grabber to allow simultaneous acquisition of all three color channels ($640 \times 480 \times 3$). Alternatively, the Photometrics SenSysTM (Roper Scientific, Inc., Tucson, AZ) camera, which is a low-light CCD having 768×512 pixels ($9 \times 9 \text{ mm}$) by 4,096 gray levels with a 1.4-MHz readout speed is also available. For fluorescence imaging, a six-position slider bar is available with filters typically used in multispectral three-color and four-color fluorescence *in situ* hybridization (FISH) sample. Several objectives are available including the Zeiss (Carl Zeiss Microimaging Inc., Thornwood, NY) PlanApo $100 \times \text{NA } 1.4$ objective, CP Achromat $10 \times \text{NA } 0.25$, Plan-Neofluar $20 \times \text{NA } 0.5$, Achroplan $63 \times \text{NA } 0.95$, Meiji S-Plan $40 \times \text{NA } 0.65$, Olympus UplanApo $100 \times \text{NA } 1.35$, Olympus UplanApo $60 \times \text{NA } 0.9$ and Olympus UplanApo $40 \times$, N.A. 0.5-1.0. The automated microscope system is controlled by proprietary software running on a PowerMac G4 computer (Apple Inc., Cupertino, CA).

5.2 Software

The software that controls the automated microscope includes functions for spatial and photometric calibration,

automatic focus, image scanning and digitization, background subtraction, color compensation, nuclei segmentation, location, and measurement, and FISH dot counting [29].

5.2.1 Autofocus

Autofocus is done by a two-pass algorithm designed to determine first whether the field in question is empty or not, and then to bring the image into sharp focus. The first pass of the algorithm examines images at three z-axis positions to determine whether there is enough variation among the images to indicate the presence of objects in the field to focus on. The sum over the image of the squared second derivatives described by Groen et al. [16] is used as the focus function $f(x)$:

$$f(x) = \sum_i \sum_j \left(\frac{\partial^2 g(x, y)}{\partial x^2} \right)^2 \quad (6)$$

A second-order difference is used to estimate the second-order derivative (Laplacian filter).

$$\frac{\partial^2 g(x, y)}{\partial x^2} \approx \frac{\Delta^2 g}{\Delta x^2} = g(i, j+1) - 2g(i, j) + g(i, j-1) \quad (7)$$

Where $g(i, j)$ is the image intensity at pixel (i, j) .

The Laplacian filter strongly enhances the higher spatial frequencies and proves to be ideal for our application. At the point of maximal focus value, the histogram is examined above a predetermined threshold to determine the presence of cells in the image.

Once the coarse focus step is complete, a different algorithm brings the image into sharp focus. The focus is considered to lie between the two z-axis locations that bracket the location that gave the highest value in the coarse focus step. A hill-climbing algorithm is then used with a “fine-focus” function based on gradients along 51 equispaced horizontal and vertical lines in the image. Images are acquired at various z-locations, “splitting the difference” and moving toward locations with higher gradient values until the z-location with the highest gradient value is found, to within the depth of focus of the optical system. To ensure that the background image of all the color channels are in sharp focus, the fine-focus value is taken to be the sum of the fine-focus function outputs for each of the three (or four) color channels.

The coarse focus routine determines the plane of focus (three frames), and is followed by a fine-focus algorithm that finds the optimal focus plane (approximately five to eight frames). The total number of images analyzed during the fine-focus routine depends upon how close the coarse focus algorithm got to the optimal focus plane. The closer the coarse focus comes to the optimal focus position, the fewer steps are required in the fine-focus routine. The autofocus technique works with any objective by specifying its numeric aperture,

which is needed to determine the depth of focus, and focus step size. It is conducted at the beginning of every scan, and it may be done for every scan position or at regular intervals as defined by the user. A default interval of ten scan positions is programmed. We found that the images are “in-focus” over a relatively large area of the slide, and frequent refocusing is not required. For an integration time of 0.5 seconds we recorded an average autofocus time of 28 ± 4 seconds. The variability in the focusing time is due to the varying number of image frames captured during the fine-focus routine. The total time for autofocus depends on image content (which will affect processing time), and the integration time for image capture.

5.2.2 Slide Scanning

The algorithm to implement automated slide scanning moves the slide in a raster pattern. It goes vertically down the user-selected area and then retraces back to the top. It moves to a predetermined fixed distance across and then starts another scan vertically downward. This process is continued until the entire user-defined area has been scanned. The step size in the X and Y directions is adjusted (depending on the pixel spacing for the objective in use) such that there is no overlap between the sequentially scanned fields.

The system was designed to implement slide scanning in two modes depending on the slide preparation. A “spread” mode allows the entire slide to be scanned, whereas a “cytospin” mode may be used to scan slides prepared by centrifugal cytology. Both the spread and cytospin modes also have the capability to allow user-defined areas (via fixed area or lasso) to be scanned. The average slide-scanning rate recorded for the system is 12 images/min. This value represents the total scanning and processing (autofocusing and image analysis) rate. Image analysis algorithms are tailored for each specific application.

6 Applications in Clinical Cytogenetics

Cytogenetics is the study of chromosomes, especially in regard to their structure and relation to genetic disease. Clinical cytogenetics involves the microscopic analysis of chromosomal abnormalities such as an increase or reduction in the number of chromosomes, or a translocation of part of one chromosome onto another. Advances in the use of DNA probes have allowed cytogeneticists to label chromosomes and determine if a specific DNA sequence is present on the target chromosome. This has been useful in detecting abnormalities beyond the resolution level of studying banded chromosomes in the microscope, and in determining the location of specific genes on chromosomes. Clinical tests are routinely performed on patients in order to screen for and identify genetic problems associated with chromosome morphology. Typical tests offered include karyotype analysis, pre- and postnatal aneuploidy screening by polymerase chain reaction (PCR) or

FISH, microdeletion and duplication testing via FISH, telomere testing via FISH, MFISH (multiplex FISH), and chromosome breakage and translocation testing. The ADIR computerized microscopy system has been applied to the following cytogenetic screening tests.

6.1 Fetal Cell Screening in Maternal Blood

Scientists have documented the presence of a few fetal cells in maternal blood, and have envisioned using them to enable noninvasive prenatal screening. Using fetal cells isolated from maternal peripheral blood samples eliminates the procedure-related risks associated with amniocentesis and chorionic villus sampling [50].

The minute proportion of fetal cells found in maternal blood can now be enriched to one per few thousand using magnetic activated cell sorting (MACS) [51], or fluorescence activated cell sorting (FACS) [52], or a combination of the two. Aneuploidies can then be detected with chromosome-specific DNA probes via FISH [53]. Microscopy-based approaches have been used to identify fetal cells in maternal blood, but the small number of fetal cells present in the maternal circulation limits accuracy and makes cell detection labor intensive. This creates the need for a computerized microscopy system to allow repeatable, unbiased, and practical detection of the small proportions of fetal cells in enriched maternal blood samples.

FISH is one of the methods currently under investigation for the automated detection of fetal cells. It is a quick, inexpensive, accurate, sensitive, and relatively specific method that allows detection of the autosomal trisomies 13, 18, and 21; X and Y abnormalities; and any other chromosome abnormality for which a specific probe is available.

We used the ADIR system to detect fetal cells in FISH-labeled maternal blood. The separated cells in enriched maternal blood were examined for gender and genetic aneuploidy using chromosome specific DNA probes via FISH. The nucleus was counterstained with DAPI ($4'$ D,6-diamidino-2-phenylindole), and chromosomes X and Y were labeled with SpectrumGreen and SpectrumOrange, respectively (Vysis Inc., Downers Grove, IL).

If the fetus is male, FISH can be used directly, with one probe targeting the Y-chromosome, and different colored probes for other chromosomes, to detect aneuploidies. An automated system can examine enough cells to locate several fetal (Y-positive) cells and then make a determination about aneuploidy in the fetus. If the fetus is female, one must analyze a number of cells that is sufficient to rule out the possibility of aneuploid fetal cells.

Specific image analysis algorithms were used to detect the cells and FISH dots, following background subtraction and color compensation. The digitized images were initially thresholded in the user-defined cell channel (generally, blue for the DAPI counterstain) to obtain binary images of cells.

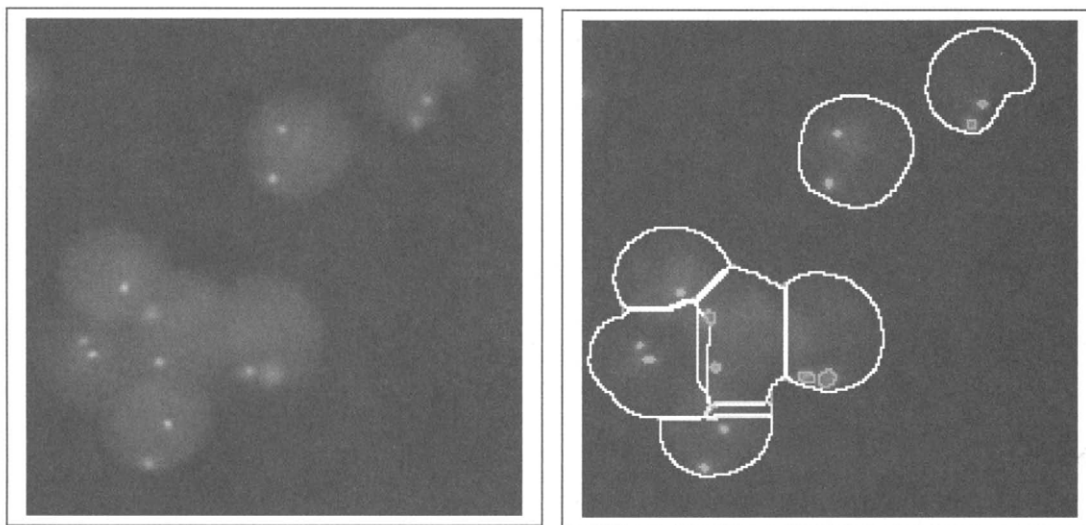


FIGURE 4 Fluorescence image of 7 female (XX) cells. Adult female blood was processed via FISH. Cells are counterstained blue (DAPI); X chromosomes are labeled in green (FITC). Results of automated image analysis are illustrated in the right panel. The software accurately detects single cells, separates touching cells, and detects the green dots in individual cells (see color insert).

The cells were then uniquely identified using a region labeling procedure [54]. The 8-connected pixel neighborhood is used to determine the pixel belonging to a certain object. Each pixel in the connected neighborhood is then assigned a unique number so that finally all the pixels belonging to an object will have the same unique label. The number of pixels in each object is computed and used as a measure of cell size. Subsequently, shape analysis is used to discard large cell clusters and noncircular objects. Further, a morphologic technique is used for automatically cutting touching cells apart. The morphologic algorithm shrinks the objects until they separate, and then thins the background to define cutting lines. A logical exclusive OR procedure then separates cells. Cell boundaries are smoothed by a series of erosions and dilations, and the smoothed boundary is used to obtain an estimate of the cellular perimeter. Performing a logical AND operation on this thresholded and morphologically processed mask with the other two red and green planes of the color compensated image yields gray-scale images containing only dots that lie within the cells. Objects are then located by thresholding in the probe color channels, using smoothed boundaries as masks. A minimum size criterion is used to eliminate noise spikes, and shape analysis is used to flag noncompact dots. The remaining objects are counted. The locations of dots found are compared with the cell masks to associate each chromosomal dot with its corresponding cell. Finally, we implemented a statistical model to determine unbiased estimates of the proportion of cells having a given number of dots. The befuddlement theory provides guidelines for dot-counting algorithm development by establishing the point at which further reduction of dot-counting errors will not materially improve the estimate [55]. This occurs when statistical sampling error outweighs dot-counting error.

Isolated cells with dots are then evaluated to determine gender and/or aneuploidy, and finally classified as fetal or maternal cells. Once the fetal cells have been identified by the automated image analysis algorithms, the stage and image coordinates of such cells are stored in a table along with the cell's morphologic features, such as area, shape factor, and dot count. The detected cells can be automatically relocated at any subsequent time by centering upon the centroid of the cells using the previously stored stage and image coordinates. The results of automated image analysis are illustrated in Fig. 4. The software accurately (a) detects single cells, (b) separates touching cells, and (c) detects the green dots in the isolated cells. The fetal cell screening system evaluation is presented in a recent publication [56].

6.2 Subtelomeric Fluorescent In Situ Hybridization for Detection of Cryptic Translocations

Subtelomeric FISH (STFISH) uses a complete set of telomere region-specific FISH probes designed to hybridize to the unique subtelomeric regions of every human chromosome. Recently, a version of these probes became commercially available (ChromoProbe MultiprobeTM T-System, Cytocell Ltd.). The assay allows for simultaneous analysis of the telomeric regions of every human chromosome on a single microscope slide, except the p-arms of the acrocentric chromosomes. It is anticipated that these probes will be extremely valuable in the identification of submicroscopic telomeric aberrations. These are thought to account for a substantial, yet previously underrecognized, proportion of cases of mental retardation in the population. The utility of these probes is evident in that numerous recent reports describe

cryptic telomere rearrangements or submicroscopic telomeric deletions [57].

6.2.1 The Subtelomeric Fluorescent In Situ Hybridization Assay

STFISH uses a special 24-well slide template that permits visualization of the subtelomeric regions of every chromosome pair at fixed positions on the slide template (Fig. 5). Each well has telomeric-region-specific probes for a single chromosome; for example, well 1 has DNA probes specific to the telomeric regions of chromosome 1, and well 24 has DNA probes specific for the Y chromosome telomeres. At present, the assay requires a manual examination of all 24 wells. When screening anomalies, first each of the 24 regions on the slide must be viewed to find metaphases. The second step involves image acquisition, followed by appropriate image labeling (to indicate the region on the slide from which the image was captured), and saving the images. This is required to identify the chromosomes correctly. The third step involves an examination of the saved images of one or more metaphases from each of the 24 regions. This examination involves the identification of the (labeled green) p-regions and the (red labeled) q-regions for each pair of chromosomes in each of the 24 regions. Finally, the last step requires the correlation of any deleted or additional p- or q-arm telomeric material within the 24 regions, to allow the interpretation of the telomeric translocation, if present. A trained cytogeneticist takes approximately 3 hours to complete reading a slide for the STFISH assay, and an additional hour to complete data analysis. Furthermore, the procedure is not only labor-intensive, but it requires trained cytogeneticists for slide reading and data interpretation. This procedure is even more tedious

in cases without prior knowledge of the chromosomal anomaly.

It is apparent that computerized microscopy can be applied to produce labor and time savings for this procedure. Automated motorized stages, combined with computer controlled digital image capture, can implement slide scanning, metaphase finding, and image capture, labeling, and saving (steps 1 and 2). This removes the tedious and labor-intensive component of the procedure, allowing a cytogeneticist to examine a gallery of stored images rapidly for data interpretation. Image analysis algorithms can also be implemented to automatically flag images that have missing or additional telomeric material (steps 3 and 4). This would further increase the speed of data interpretation. Finally, automated relocation capability can be implemented, allowing the cytogeneticist to perform rapid visual examination of the slide for any of the previously recorded images.

We recorded a slide scanning time (including autofocusing, scanning, and image analysis) of four images/min ($\sim 0.04 \text{ mm}^2/\text{min}$) for an integration time of 0.5 seconds. The slide-scanning algorithm was designed to scan the special Cytocell, Inc., template slide that is used for the STFISH. As seen in Fig. 5, the template slide is divided into 24 squares (three rows of eight) labeled from 1 to 22, X and Y. Each square in the grid is scanned, and the metaphases found in each square are associated with the corresponding chromosome label. This is accomplished by creating a lookup table that maps each square in the grid to fixed stage coordinates. The stage coordinates of the four vertices of each square are located and stored.

6.2.2 User Interface

The user-interface for the newly designed slide-scanning algorithm is presented in Fig. 6. The 24 well regions of the Cytocell template slide are mapped to the corresponding stage coordinates as shown in Fig. 6. The cross-hair (seen in region 12) indicates the current position of the objective. The user can select a particular slide region, or a range of slide regions, as desired for scanning. For each selected region, scanning begins at the center and continues in a circular scan outward, toward the periphery. This process is continued until the entire selected region is scanned or a predefined number of metaphases have been found. The default is to scan the entire slide, starting at region 1 and ending at region 23 (for female specimens) or 24 (for male specimens), with a stop limit of five metaphases per region. For example, at the end of the default scan, the image gallery would have 120 metaphase images for a male specimen. The step size in both the X and Y directions can be adjusted (depending on pixel size, as dictated by the objective in use) so that there is no overlap between sequential scan fields. This is controlled by the X- and Y-axis factors shown in the user interface in Fig. 6.

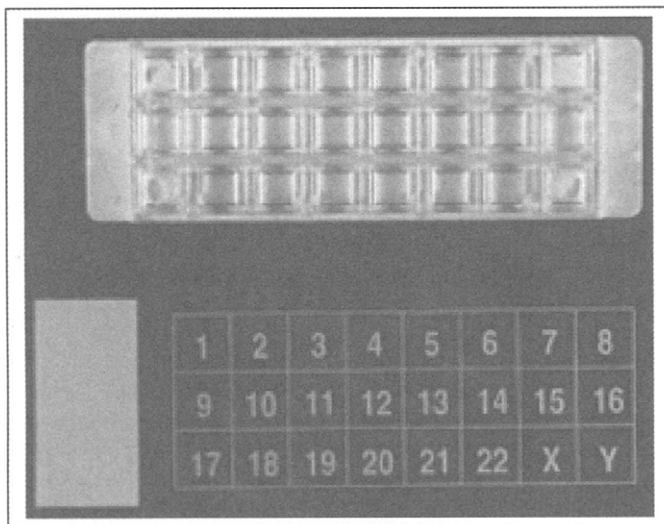


FIGURE 5 Illustration of the “Multiprobe®” coverslip device (top) divided into 24 raised square platforms and the “template microscope slide” (bottom) demarcated into 24 squares.

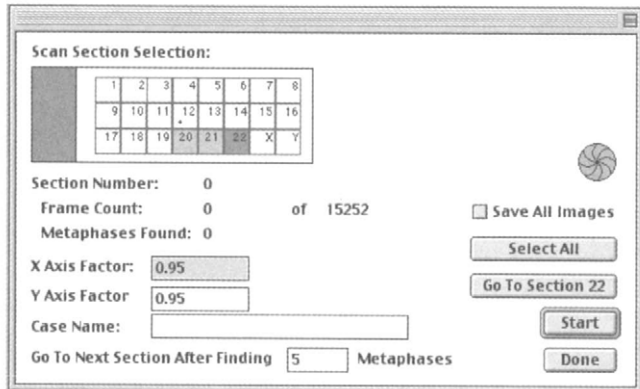


FIGURE 6 User interface for automated scanning of the Cytocell Multiprobe[®] template microscope slide. The user can select a region to scan at the click of a mouse button (Ex: regions 20, 21 and 22 were selected above). Either the entire selected region can be scanned, or the user can define the number of metaphases per region (Ex: 5 Metaphases, as shown above). Scanning then continues with the next selected region. The X-axis and Y-axis factors adjust the scanning step-size in X and Y, and may be used to capture overlapping regions to avoid the loss of cells that fall between adjacent image frames (see color insert).

6.2.3 Metaphase Finding

Image analysis capability for this application includes locating the metaphases in the images. The software first uses gray level thresholding and boundary tracking algorithms to find objects in the image. The isolated objects are then classified using a set of user-defined parameters, to identify metaphases. The key classification parameters include the size and shape of the objects, clustering of similar objects in a group, and the number of objects in a group. This works because chromosomes in a metaphase are typically rodlike and are clustered together in groups of approximately 46.

Figure 7 shows the user interface for metaphase finding, with default object parameters for images captured with a 100 \times objective. These parameter values, when tested on more than ten images, accurately identified the all metaphases

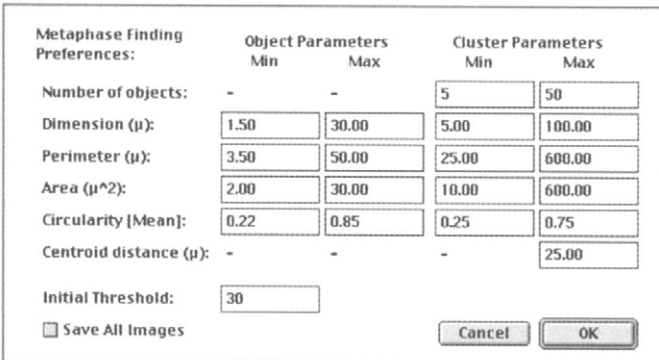


FIGURE 7 User-interface for automated metaphase finding preferences. The object parameters were empirically determined by ADIR to operate best on typical metaphase specimens captured using a 100X objective.

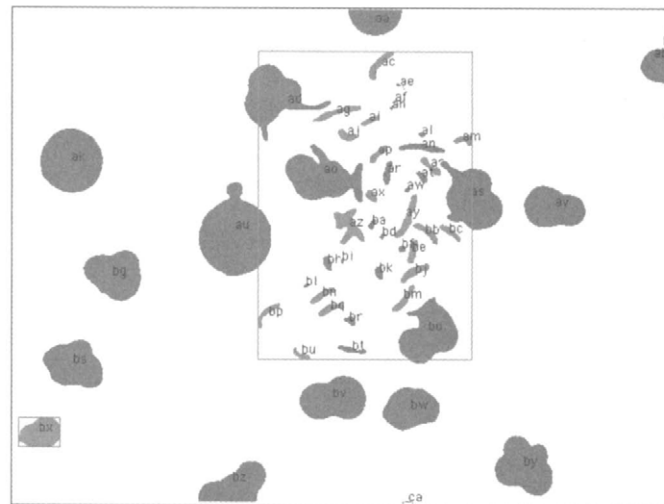


FIGURE 8 The output of the metaphase finding algorithm. The isolated objects are labelled aa-az, ba-bz, and ca (total 53 objects), and then classified using the parameters described in Fig. 7. The objects in green were classified as objects of a cluster, while red objects are rejected. A cluster of objects outlined by a green box is identified as a metaphase, while cluster objects outlined by a red box are rejected (see color insert).

therein. The result for a representative metaphase image appears in Fig. 8. The objects shown in green were selected as members of a cluster, and the clustering algorithm rejected the objects shown in red. The green box encloses the cluster of objects identified as a metaphase. Red boxes show clusters that were rejected (see the lower left corner in Fig. 8). Metaphases located at a distance of 15 mm from the boundaries of the squares are also discarded to avoid attempting to analyze metaphases that overlap two neighboring squares. Every metaphase located in an individual square on the Cytocell slide is assigned to a group numbered like the square on the template slide. Images in which metaphases are found are labeled according to their slide region and are stored in an image gallery. These metaphases can be relocated automatically later, using previously stored stage and image coordinates. The automatically identified metaphases are then visually examined for the detection of subtelomeric rearrangements. Figures 9 and 10 show images of the subtelomeric assay. This specimen has a distal monosomic 2q deletion and is trisomic for distal 17q. The subtelomeric regions on the shorter arms (p) are labeled green with FITC, and the subtelomeric regions on the longer arms (q) are labeled red using Texas Red. As seen in Fig. 9, chromosome 2 is deleted for distal q. Figure 10 shows trisomy for distal 17q, with a cryptic translocation of distal 17q on chromosome 2.

6.3 Detection of Gene Duplications

Recent studies have shown that chromosomal deletions and duplications result in human diseases with complex phenotypic abnormalities [58–59]. The current understanding is

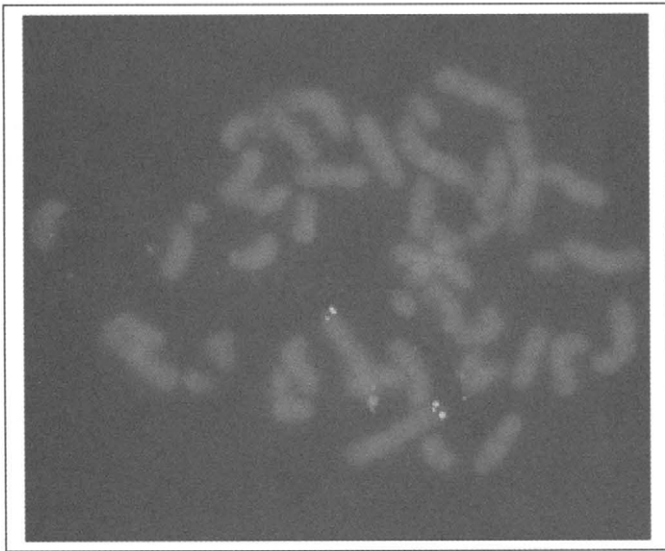


FIGURE 9 FISH was performed using subtelomeric DNA probes for chromosome 2. The q-arms are labelled red (Texas Red) and the p-arms are labeled green (FITC). This specimen is deleted for distal 2q (monosomic). Subtelomeric FISH was performed using the Chromoprobe Multiprobe® T System from Cytocell Ltd. Imaging was performed using the ADIR computerized microscopy system (see color insert).

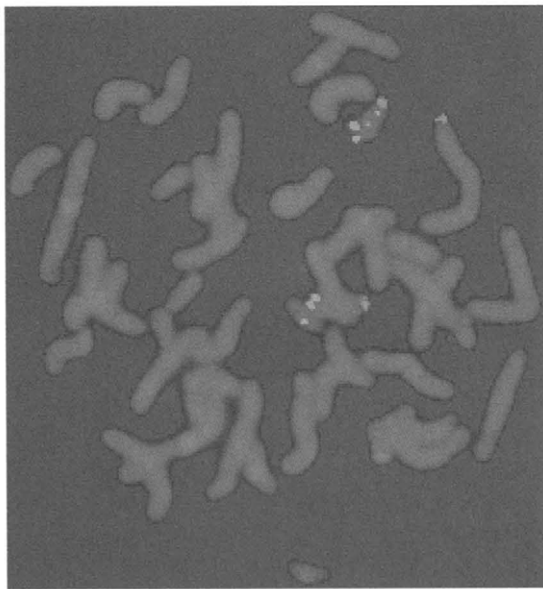


FIGURE 10 FISH was performed using subtelomeric DNA probes for chromosome 17. The q arms are labelled red (Texas Red) and the p arms are labelled green (FITC). The specimen is trisomic for distal 17q, and carries a cryptic translocation (derivative 2). Subtelomeric FISH was performed using the Chromoprobe Multiprobe® T System from Cytocell Ltd. Imaging was performed using the ADIR computerized microscopy system (see color insert).

that duplications of segments of the human genome may eventually be shown to be responsible for many human traits [60]. Following the recent sequencing of the human genome, a future task of the human genome project is to delineate genome architectural features, such as low-copy

and region-specific repeats (duplications). The eventual identification of these may enable prediction of several regions susceptible to rearrangements associated with genomic disorders. However, screening methods for genetic anomalies that use FISH, especially duplication analysis, have not advanced beyond manual screening of specimens. We used ADIR system for computerized microscopy to support fast, accurate, and inexpensive screening of gene duplications. Our approach was to use readily available DNA probes for the specific disorders such as (a) neuropathies: Charcot-Marie-Tooth disease (*CMT1A*) and hereditary neuropathy with pressure palsies (*HNPP*); (b) neurologic disorders: Pelizaeus-Merzbacher disease (*PMD*) and X-linked spastic paraplegia (*SPG2*), (c) muscular wasting disorders: Duchenne (*DMD*) and Becker muscular dystrophy (*BMD*); and (d) contiguous-gene syndromes: Smith-Magenis syndrome (*SMS*), for interphase FISH, followed by automated genetic screening to detect gene duplications.

6.3.1 Dot-Finding

The ADIR system software was tailored for this particular application to perform the following tasks. After an image is acquired, it was to be analyzed to identify nuclei and to detect dots. This involves the following four steps: (a) Find the nucleus objects, and find the dot objects within the nucleus; (b) determine if each dot object represents a single FISH signal or multiple signals; (c) measure the separation-distance between duplicated dots; (d) classify the isolated dots as single, double, split or overlapping; (e) count the dots; and (f) generate a report. The algorithms for cell and dot finding are described earlier in the fetal cell project. Specialized algorithms were developed to identify duplicated gene signals.

We implemented the following algorithm to separate individual neighboring dots and to measure the distance between the two dots. Following the dot finding algorithm, we initially determined the number of dot objects for the target fluorophore (which labeled the gene of interest). In cells carrying a duplication, the nuclei would have a total of three FISH signals for the target gene, of which two signals would occur on the abnormal chromosome (indicating a duplication), and one signal would occur on the normal chromosome. The shape of each dot object was initially measured (using existing shape analysis algorithms), to determine if it is a single or double dot. If the boundary of the dot had low eccentricity, the dot was initially tagged as a single dot. If the eccentricity was relatively high, the object had a higher probability of being a double dot. If the cell nuclei had three dot objects for the target gene, we initially isolated the two objects that were tagged as potential single dots, and were nearest to each other to represent FISH signals on the abnormal chromosome. This was achieved by determining the centroid of each dot object [54], as a measure of its spatial position in the cell nuclei. A subimage of the dot objects was

then obtained by cropping a square region enclosing the FISH signals. Figure 11A shows a cropped image of two FISH signals.

6.3.2 Surface Fitting

We obtain morphologic and image features for the dot objects by surface fitting, using the sum of two rotated gaussian surfaces as a model. The sum of two rotated Gaussian surfaces was modeled as follows:

$$\begin{aligned} f(x_a, y_a, A_a, x_{a0}, y_{a0}, \sigma_{ax}, \sigma_{ay}, \theta_a, x_b, y_b, A_b, x_{b0}, y_{b0}, \sigma_{bx}, \sigma_{by}, \theta_b) \\ = A + B \end{aligned}$$

Where

$$A = \exp \left[- \frac{[(x_a \cos \theta_a - y_a \sin \theta_a) - (x_{a0} \cos \theta_a - y_{a0} \sin \theta_a)]^2}{2\sigma_{ax}^2} \right. \\ \left. - \frac{[(x_a \sin \theta_a + y_a \cos \theta_a) - (x_{a0} \sin \theta_a + y_{a0} \cos \theta_a)]^2}{2\sigma_{ay}^2} \right] \quad (9)$$

And

$$B = \exp \left[- \frac{[(x_b \cos \theta_b - y_b \sin \theta_b) - (x_{b0} \cos \theta_b - y_{b0} \sin \theta_b)]^2}{2\sigma_{bx}^2} \right. \\ \left. - \frac{[(x_b \sin \theta_b + y_b \cos \theta_b) - (x_{b0} \sin \theta_b + y_{b0} \cos \theta_b)]^2}{2\sigma_{by}^2} \right] \quad (10)$$

In the equations above, A is the amplitude, x_0, y_0 the position, and σ_x and σ_y , the standard deviations (radii) in the two directions, and x, y , are surface points, and θ is the angle of rotation with respect to the X-axis. These parameters are used with the subscript a or b to represent the two Gaussian surfaces. A least squared minimization of the mean squared error was performed using the quasi-Newton minimization technique [61]. To recover the surface we estimated the following 12 parameters:

$$A_a, x_{a0}, y_{a0}, \sigma_{ax}, \sigma_{ay}, \theta_a, A_b, x_{b0}, y_{b0}, \sigma_{bx}, \sigma_{by}, \text{ and } \theta_b$$

The image data points from the subimage containing the dot objects (Figure 11A) were used as input points for the minimization routine. Initial estimates for the size parameters were obtained from the input data points, as follows. The centroid of the dot objects was used as an estimate for (x_0, y_0) , the average image intensity was used to estimate A , the angle of rotation was set to an initial value of 45 degrees, and the standard deviations (σ) in the x , and y directions were set to a value of 1.0. The minimization was performed using a constraint tolerance (CTOL) of 0.001, and a convergence tolerance (TOL) of 0.001. The value of CTOL controls the precision of the solution. The larger the value, the less precise the solution may be. For smaller values of CTOL, a more

precise solution may be found, but the processing time is increased. The value of TOL controls the duration of an iteration. Typically, we were able to estimate the parameters with negligible error values computed as the square root of the sum of squared residuals (computed value—expected value).

For double dots, the estimated parameters for A and B (Equation 8) differ, and may then be used to represent two single dots that are each modeled as a two-dimensional gaussian surface. If surface-fitting procedure is performed on actually a single (elliptical) dot, then the estimated parameters from the two gaussian surfaces in the model have equal, σ_x and σ_y values, and their position (x, y) was nearly equal (i.e., within two or three pixels of each other).

The performance of the surface-fitting algorithm is illustrated in Fig. 11. An image of FISH signals (dots) and its corresponding surface and contour plots are illustrated in inserts A and B, respectively. A contour plot of the surface is presented in Fig. 11C. Surface fitting was performed to obtain the model parameters, and inserts D and E show the surface plot and contour of the estimated model. Figure 11F presents the image that was reconstructed using the estimated parameters from the surface fitting.

We tested the algorithm and it performed successfully in all the cases tested. Overall, the performance of the algorithm was optimal, except for poor quality images. For, images that had an extremely low signal-to-noise ratio, the iteration procedure took slightly longer to converge to the solution resulting in a 1% to 2% reduction in the processing speed. Similarly, the single dot (from the normal homologous chromosome) was modeled using a single 2D rotated gaussian to compute its size and integrated intensity.

6.3.3 Ellipse Fitting

To compute the separation distance between double dots, the boundary for each dot was computed using the parameters estimated from the surface-fitting algorithm. This was achieved by modeling each dot as an ellipse. The following equation was used to model a single rotated ellipse.

$$f(x, y) = \frac{[(x \cos \theta - y \sin \theta) - (x_0 \cos \theta - y_0 \sin \theta)]^2}{2\sigma_x^2} \\ + \frac{[(x \sin \theta + y \cos \theta) - (x_0 \sin \theta + y_0 \cos \theta)]^2}{2\sigma_y^2} \quad (11)$$

The estimated values for $x_0, y_0, \sigma_x, \sigma_y$, and θ obtained from the surface modeling were used in the equation above, and the equation was solved to compute the boundary points by setting $f(x, y)$ to the value of 1.0. Figure 12A and B illustrates the boundary points obtained for the sample image presented in Fig. 11. The next step was to compute the separation distance between two dots. The procedure is illustrated in

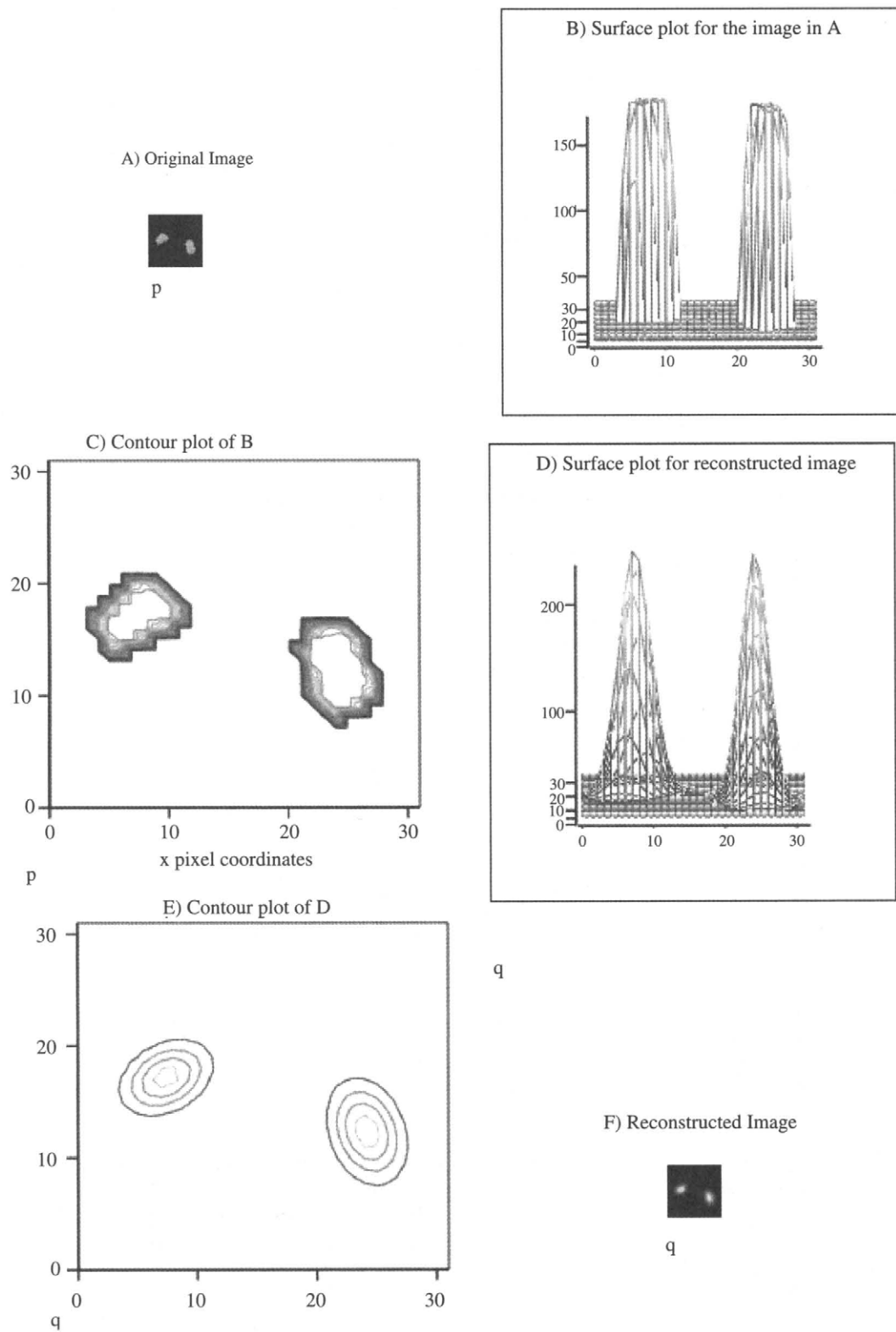


FIGURE 11 Surface fitting using the sum of two rotated Gaussians as a model. (A) Original Image, (B) surface plot of (A), (C) contour plot of (B), (D) surface plot of reconstructed image, (E) contour plot of (D), and (F) reconstructed image (see color insert).

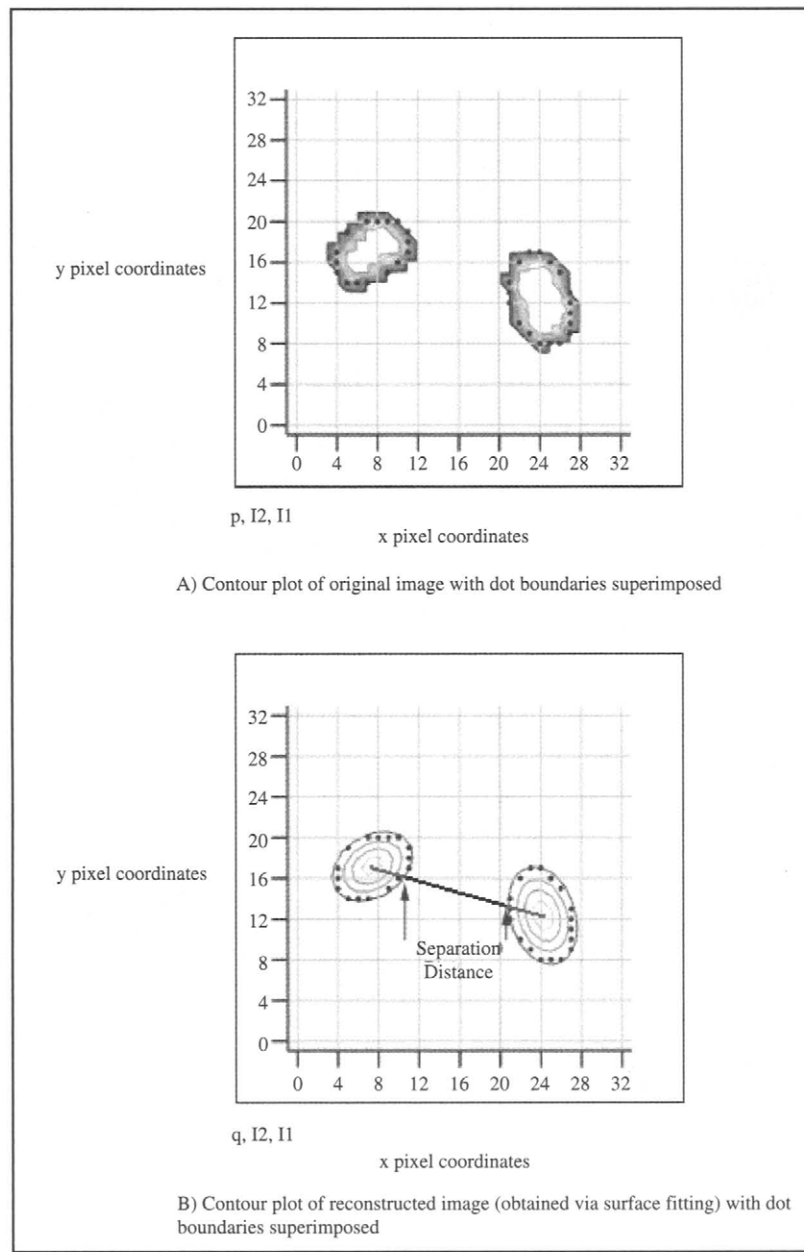


FIGURE 12 Automated measurement of separation distance between duplicated dots (see color insert).

Fig. 13. Briefly, the line segment joining the centroids of the two dots was computed as follows:

$$y = \frac{(x - x_1)(y_1 - y_2)}{(x_1 - x_2)} + y_1 \quad (12)$$

This is called the peak-to-peak distance (PP). Then the point of intersection of PP with the boundary of each of the dots was determined by simultaneously solving Equations (11) and (12). Segment PP intersects each dot boundary at two points (4 points total). The point of intersection closest to the

mid-point of segment PP was chosen for each dot [shown as (ix_1, iy_1) , and (ix_2, iy_2) in Fig. 12]. Then the shortest distance (SD) was computed as the length of the line segment joining (ix_1, iy_1) and (ix_2, iy_2) using the following equation.

$$SD = \sqrt{(ix_1 - ix_2)^2 + (iy_1 - iy_2)^2} \quad (13)$$

The separation distance was then normalized with respect to the size of the cell (cell radius) to obtain a relative measure of the distance. Finally, the total integrated fluorescence intensity, and average intensity for each dot were computed

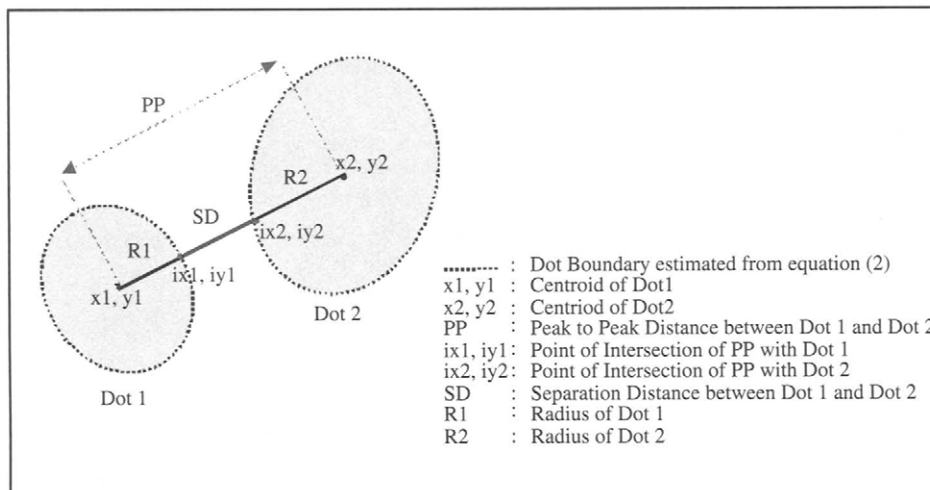


FIGURE 13 Schematic illustrating the computation of the separation distance (see color insert).

using intensity values of all pixels with the boundary. The separation distance and the average fluorescence intensity were then used to classify the dots as described below.

6.3.4 Multiple Dots

In gene duplication studies, it is important to determine whether a gene is duplicated or single. Duplicated genes are represented in FISH images, as two dots of the same color that are separated by a distance greater than or equal to the diameter of a single dot. We developed image analysis algorithms to classify dots and to determine the separation distance between the dots.

FISH dots can occur as touching dots, split dot signals, overlapping dots, or separated dots. The measured values of the separation distance (SD), average intensity (IS), and diameter (DS) for single signals, and average intensity I_1 and I_2 for duplicated signals was used to classify the dots. The single dot represents the unduplicated gene on the homologous chromosome, and double dots represent the target pair of dots to be classified. Typically, for touching dots the separation distance is zero. A FISH signal is sometimes smeared so that a single dot splits into (appears as) two dots. This is called a split signal. In this case, one dot is usually smaller than the other. The separation distance for split dots is less than one-fourth the size of the single dot, and the intensity of both or at least one dot is less than the intensity of the single dot. During the S phase of the cell cycle during DNA synthesis, chromosomes are replicated and thus two dots are seen in FISH images. These are called replicated signals. The distance between replicated dots is typically small, because the separation distance is proportional to the width of the sister chromatids. However, since the gene locus is itself replicated the intensity and size of each dot is equal to that of the single dot. Finally, duplicated signals are used to represent true gene duplication. These dots are well separated from each other

such that the separation distance between the dots is greater than or equal to the half the size of the single dot, and each has a size and intensity equal to that of a single dot. These criteria are illustrated and outlined in Fig. 14. The diameter and intensity of the signal (on the normal chromosome) are chosen for the single dot parameters. Intensity values are considered significant only if the intensity values change by more than 40% (for either an increase or reduction). This is because several other factors such as background noise, homogeneity of the light source, type and concentration of the probe affect the intensity value. Thus, small changes were neglected and only large variations in intensity are considered while classifying the signals. Finally, the ratio of the separation distance to the diameter of a single dot (SD/DS) was used to classify the signals based on the criteria outlined in Fig. 14. If this ratio takes values equal to 0.5, 1.0, 2.0, 3.0,... this indicates that one half, one, two, three,... dots can occupy the space between the duplicated genes. The dots were classified based on two parameters, the ratio SD/DS, and the intensity ratio $(I_1 + I_2)/IS$. Split signals have values of $SD/DS \approx 0.0 - 1.0$, and $IS \approx I_1 + I_2$, replicated signals have a SD/DS value less than 0.0 to 0.5, and $(I_1 + I_2)/IS \approx 2.0$, and duplicated signals have a SD/DS ratio ≥ 0.5 , and $(I_1 + I_2)/IS \approx 2.0$.

Figure 15 presents an image of a cell showing a duplication pattern for CMT1A. The PMP22 cosmid contig was labeled with digoxigenin and detected with anti-digoxigenin conjugated to rhodamine, which fluoresces red. The FL1 cosmid contig was labeled with biotin and detected with avidin conjugated to FITC, which fluoresces green. FL1 cosmid was used as an internal control to facilitate chromosome identification, and to check hybridization efficiency. In each interphase nucleus, the normal chromosome 17 displays one green and one red signal. In cells carrying the duplication, the abnormal chromosome 17 shows one green signal and two red signals (Fig. 15).

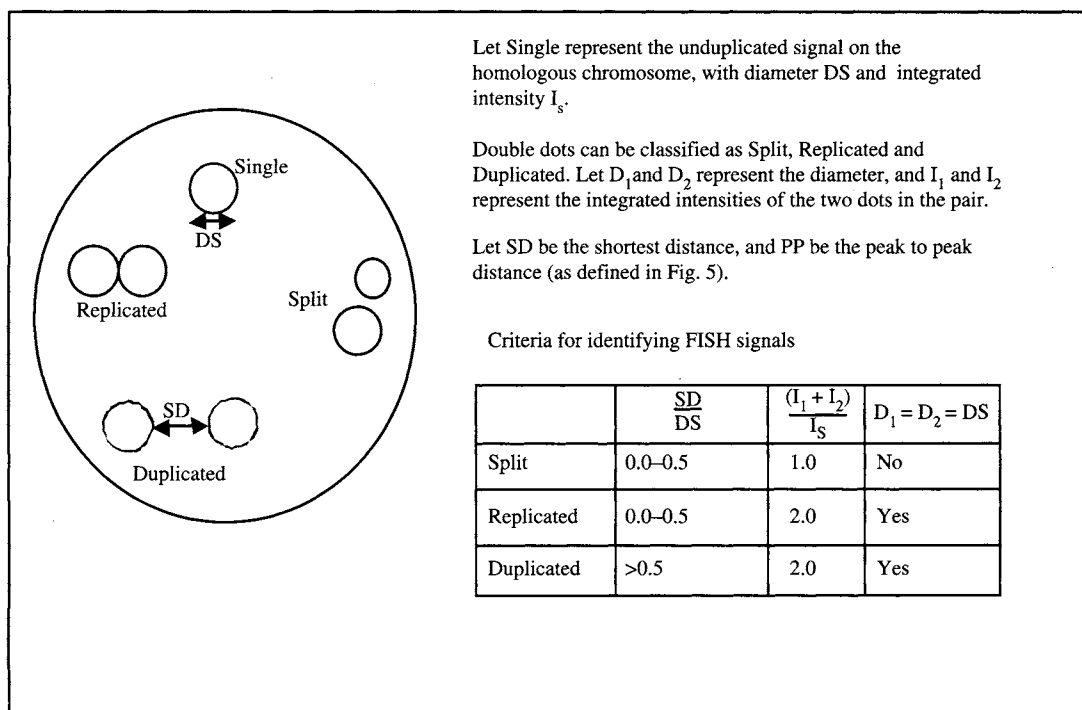


FIGURE 14 Criteria for classifying split, replicated and duplicated signals (see color insert).

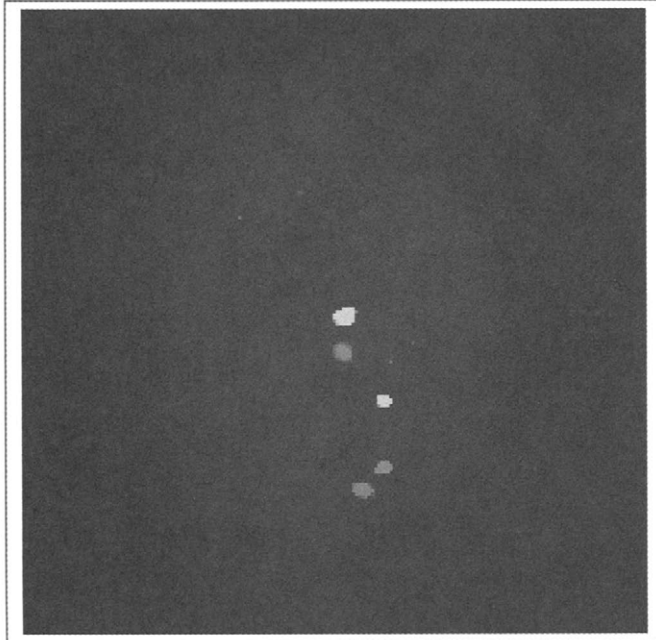


FIGURE 15 Representative cell for CMT1A showing a duplication pattern. The PMP22 cosmid contig was labelled with digoxigenin and detected with anti-digoxigenin conjugated to rhodamine, which fluoresces red. The FLI cosmid contig (internal control) was labelled with biotin and detected with avidin conjugated to FITC, which fluoresces green. In each interphase nucleus the normal chromosome 17 displays one green and one red signal. A duplication is seen here with the abnormal chromosome 17 showing one green signal and two red signals (see color insert).

6.3.5 Performance

The results of our study are presented in Table 1. Ten CMT1A patient samples were analyzed, with three to 15 cells per sample. An average value of 1.46 ± 0.43 , and 2.21 ± 0.45 was measured for SD/DS and $I_1 + I_2/IS$, respectively. The SD between duplicated dots is of a known size (i.e., 1.5 MB), whereas since the signal is duplicated, the intensity of each replicated signal should match that of a single gene giving an intensity ratio of 2.0. The within and across sample variability for SD/DS was found to be $\sim 30\%$, and $\sim 15\%$, respectively. The within and across sample variability for $I_1 + I_2/IS$ was found to be $\sim 22\%$, and $\sim 20\%$, respectively. The automated analysis was able to correctly identify 10/10 (100%) of the samples as gene duplications.

6.4 Four-Color Fluorescent In Situ Hybridization for Aneuploidy Screening

The AneuVysion Assay (Vysis Inc., Downers Grove, IL) is a prenatal test that provides rapid (24–48 hour) detection of trisomy 13, 18, and 21 (Down syndrome) and aneuploidy of sex chromosomes X and Y. The probe mixture for chromosomes 18 (SpectrumAquaTM D18Z1, alpha satellite DNA (18p11.1-q11.1)), X (SpectrumGreenTM DXZ1, alpha satellite DNA (Xp11.1-q11.1)) and Y (SpectrumOrangeTM DYZ3, alpha satellite DNA (Yp11.1-q11.1)) is a three-color

TABLE 1 Results using CMT1A specimens with a known 1.5-MB duplication

No.	Signal Percentage (N ≈ 100)		# of cells	Automated Analysis for Separation Distance (SD) of Duplicated Signals (Dot ₁ , Dot ₂)							
				Radius of Signals (μ)			Intensity of Signals (μ)			SD/DS	I ₁ + I ₂ /I _S
	3 dots	2 dots		Single	Dot ₁	Dot ₂	I _S	I ₁	I ₂		
1.	70	30	15	2.0	1.5	1.7	42.9	39.1	41.5	1.4 ± 0.4	2.0 ± 0.7
2.	80	20	5	1.3	1.3	0.9	18.7	30.2	16.0	1.5 ± 0.3	2.2 ± 0.4
3.	80	20	9	1.6	1.3	1.4	26.0	25.3	25.4	1.3 ± 0.4	2.0 ± 0.4
4.	80	20	10	1.5	1.1	1.2	27.3	29.4	31.7	1.4 ± 0.3	2.2 ± 1.0
5.	70	30	3	1.6	1.5	1.4	51.2	39.7	45.3	1.6 ± 0.3	1.6 ± 0.5
6.	70	30	3	2.9	2.9	2.5	100.4	79.5	93.7	1.1 ± 0.6	1.7 ± 0.1
7.	80	20	4	2.2	2.1	1.7	110.4	112.5	108.1	1.5 ± 0.5	2.0 ± 0.5
8.	74	26	3	2.0	1.8	2.3	107.7	118.6	111.8	1.0 ± 0.4	2.1 ± 0.2
9.	74	26	3	2.1	2.9	2.0	31.0	50.5	49.0	1.7 ± 0.5	3.2 ± 0.2
10.	70	30	5	3.2	2.5	2.1	134.7	144.8	138.4	1.7 ± 0.6	2.2 ± 0.5
Average								1.46 ± 0.43		2.12 ± 0.45	

FISH assay. This results in four-color images, using aqua, green, and orange for the dots, and blue for the cell nuclei. The ADIR system uses a cooled three-chip RGB camera and a 24-bit frame grabber board, allowing simultaneously capture of three color channels in a single video frame time. Use of the cooled three-chip camera facilitates the capture of high-resolution RGB images that are free of color aliasing. The ADIR system can capture four-color FISH images (blue cells with red, green, and aqua signals). Typically, when digitizing four-color images with an RGB camera, one of the three color channels captures the fourth color in a second scan. For FISH samples that use, for example, a blue counterstain, with SpectrumAqua, SpectrumGreen, and SpectrumOrange labeling chromosomes 18, X, and Y, respectively, the SpectrumOrange fluorophore is imaged in the red channel, the SpectrumGreen fluorophore in the green channel, and both DAPI and SpectrumAqua are imaged in the blue channel.

6.4.1 Image Acquisition

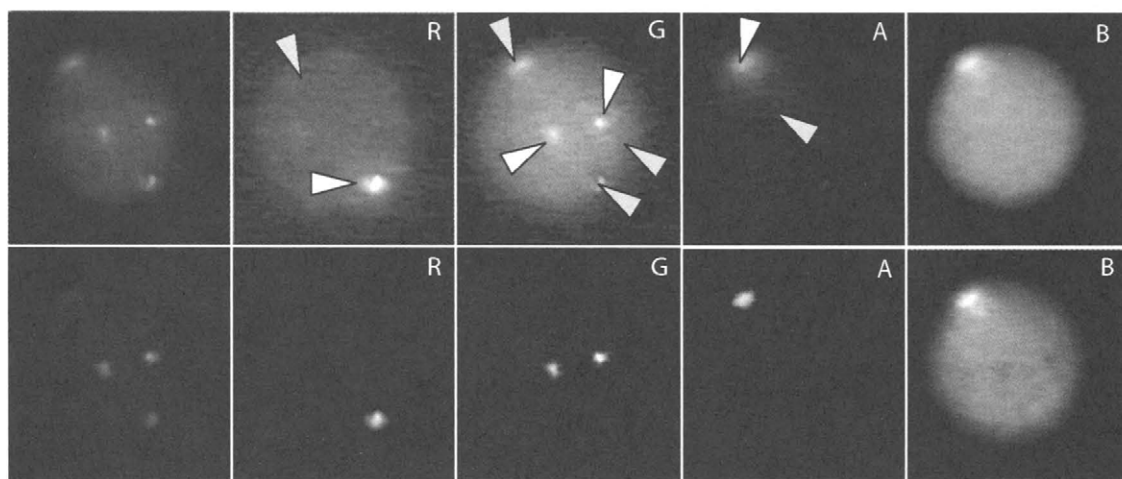
The ADIR system uses a novel solution to allow four-color sample processing using an RGB camera. The system employs a filter wheel fitted with a 420-nm long-pass (LP) filter in the excitation path, and it captures RGB images using a Quad-band (red, green, blue, aqua) optical filter set. In this setup, the Quad filter is stationary, and image capture is done in two frame-grab cycles. First, the LP filter is positioned in the light path to block DAPI excitation, and the red, green, and aqua channels are captured simultaneously. Next, the LP filter automatically moves out of the excitation path, and the DAPI image is acquired in the blue channel. Thus, we automatically capture four-color images with an RGB camera in two video frame times. The resulting digital image is stored with four channels, one for each color.

6.4.2 Spectral Overlap

Since each of the four fluorophores is imaged in a separate channel, the problem of analyzing different color dots occurring at the same X-Y location is eliminated. However, to achieve total discrimination between different color signals, the effects of spectral overlap should be minimized. As seen in Fig. 16 (top panel), the RGBA image clearly shows the blue nucleus, and the red, green, and aqua dots. The individual red, green, blue, and aqua components of the image are shown. As seen in each component image, in addition to the true color for each channel (white arrows) there is color bleed-through that occurs from neighboring spectral regions (yellow arrows). This is due to the unavoidable overlap among fluorophore emission spectra and RGB camera sensitivity spectra. The RGBA image was corrected to remove the overlap and separate the fluorophores using color compensation [32]. Figure 16 (bottom panel) shows the results of color compensation. The spectral bleed-through is effectively removed, and the different color dots are clearly separated in the individual color component images. Thus, using a 3CCD color camera, along with the background subtraction and color compensation algorithms discussed above, we obtain good spectral separation with rapid image capture. Similarly, appropriate filter optics, used in conjunction with image processing, allows the capture of multicolor images. Following image capture, the cell and dot finding algorithms described above are applied to implement automatic aneuploidy screening.

6.5 Thick-Specimen Imaging

Automated microscope instruments almost uniformly do their analysis on 2D images, and their ability to handle thick-specimens is severely limited. In thick-specimen preparations, structures that fall above or below the focal plane are



Color compensation applied to an image of a FISH labelled lymphocyte. The nucleus is counterstained with DAPI, and dots are labelled with red (chromosome Y), green (chromosome 21), and aqua (chromosome X). The original image and individual red (R), green (G), and (A) and blue (B) channels are shown in the top panel. The compensated image and its component channels are shown in the bottom panel. The spectral overlap and its effective removal via color compensation is evident in the green channel image.



Intensity profile of a line segment (white) through aqua, green, and red dots. Graph A presents the intensity profile before processing, and Graph B presents the intensity profile of the compensated image.

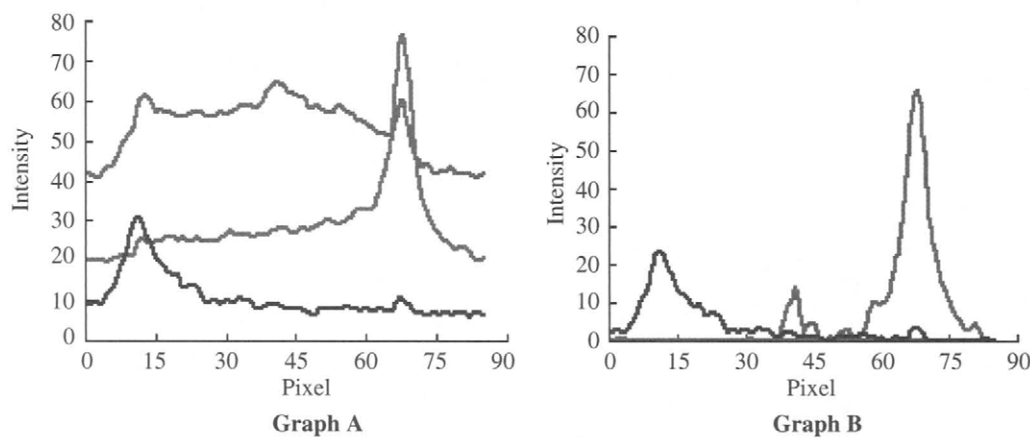


FIGURE 16 A 4-color image captured using a RGB camera and color compensation (see color insert).

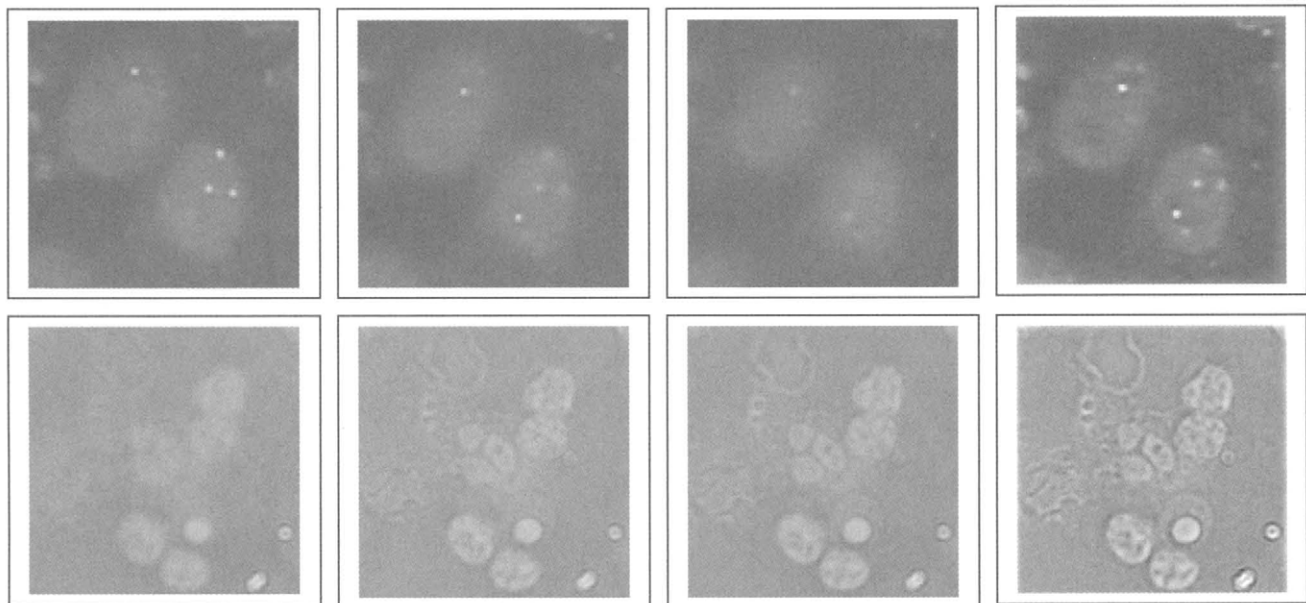


FIGURE 17 Deblurring. The top row shows images of FISH-labeled lymphocytes. The left three images are from an optical section stack taken one micron apart. The right image is the middle one deblurred. The inplane dots are brighter, while the out-of-plane dots are removed. The bottom row shows transmitted images of May-Giemsa stained blood cells. The left three images are from an optical section stack taken one-half micron apart. The rightmost image is the middle one deblurred (see color insert).

obscured or lost. The reliability of automated microscopy could be highly increased, if the thick-specimen limitation were resolved. We have developed a technique for enhancing the image content available in microscope images of thick sections by performing optical section deblurring, followed by image fusion using wavelet transforms.

6.5.1 Deblurring

Weinstein and Castleman [62] pioneered the deblurring of optical section images using a simple method that involves subtracting adjacent plane images that have been blurred with an appropriate defocus point spread function, given by:

$$f_j \approx g_j - \sum_{i=1}^M (g_{j-i} * h_{-i} + g_{j+i} * h_i) * k_0 \quad (14)$$

where f_j is the specimen brightness distribution at focus level j , g_j is the optical section image obtained at level j , h_i is the blurring psf due to being out of focus by the amount i , k_0 is a heuristically designed high pass filter, and the $*$ represents the convolution operation.

Thus one can partially remove the defocused structures by subtracting $2M$ adjacent plane images that have been blurred with the appropriate defocus point spread function and convolved with a suitable high pass filter k_0 . The filter, k_0 , and the number, M , of adjacent planes must be selected to give good results. While this technique cannot recover the specimen

function exactly, it does improve optical section images at reasonable computational expense. It is often necessary to use only a small number, M , of adjacent planes to remove most of the defocused information. Figure 17 shows images from (A) transmitted light microscopy, (B) fluorescence microscopy that have been deblurred using optical sections above and below at a Z -interval of $1 \mu\text{m}$. While this technique cannot recover the specimen function exactly, it does improve optical section images at reasonable computational expense.

6.5.2 Image Fusion

One effective way to combine a set of deblurred optical section images into a single 2D image containing the detail from each involves the use of the wavelet transform [8]. A linear transformation is defined by a set of basis functions. It represents an image by a set of coefficients that specify what mix of basis functions is required to reconstruct that image. Reconstruction is effected by summing the basis functions in proportions specified by the coefficients. The coefficients thus reflect how much each of the basis functions resembles a component of the original image. If a few of the basis functions match the components of the image, then their coefficients will be large, and the other coefficients will be negligible, yielding a very compact representation. The coefficients that correspond to the desired components of the image can be increased in magnitude, prior to reconstruction, to enhance those components.

6.5.3 Wavelet Design

A wavelet transform is a linear transformation in which the basis functions (except the first) are scaled and shifted versions of one function, called the “mother wavelet.” If the wavelet can be selected to resemble components of the image, then a compact representation results. There is considerable flexibility in the design of basis functions. Thus, it is often possible to design wavelet basis functions that are similar to the image components of interest. These components, then, are represented compactly in the transform by a relatively few coefficients. These coefficients can be increased in amplitude, at the expense of the remaining components, to enhance the interesting content of the image. Fast algorithms exist for the computation of wavelet transforms.

Mallat’s iterative algorithm for implementing the one-dimensional discrete wavelet transform (DWT) [64] is shown in Fig. 18. In the design of an orthonormal DWT, one begins with a “scaling vector,” $h_0(k)$, of even length. The elements of the scaling vector must satisfy certain constraints imposed by invertibility. For example, the elements must sum to $\sqrt{2}$, their squares must sum to unity, and the sum of the even-numbered elements must equal the sum of the odds [64]. From $h_0(k)$ is generated a “wavelet vector”

$$h_1(k) = \pm(-1)^k h_0(-k) \quad (15)$$

These two vectors are used as discrete convolution kernels in the system of Fig. 18 to implement the DWT. For example, all possible four-element orthonormal scaling vectors are specified by

$$h_0 = [c_1 c_3 \ c_1 \ c_2 - c_2 c_3]^T \quad (16)$$

where

$$c_3 = \frac{\sqrt{1 - (c_1^2 + c_2^2)}}{\sqrt{c_1^2 + c_2^2}} \quad (17)$$

and c_1 and c_2 are free-choice parameters. All even-length orthonormal scaling vectors, and biorthogonal scaling vectors of any length, can be similarly parameterized.

Mallat’s algorithm leads to the “cascade” algorithm of Daubechies [63, 64], which is a simple method for constructing the basis functions that correspond to specified scaling and wavelet vectors. With these tools, it is then simple to specify and design wavelet transforms with desired properties. Given parameterized scaling and wavelet vectors, first select the parameter values (e.g., c_1 and c_2 , above) and then use the cascade algorithm to construct the corresponding scaling function and basic wavelet. These show the form of the basis functions of that wavelet transform. Repeat the process using different parameter values until the desired basis function shape is attained. Then use $h_0(k)$ and $h_1(k)$ in the 2D version of Mallat’s algorithm to implement the wavelet transform and its inverse.

6.5.4 Wavelet Fusion

Image fusion is the technique of combining multiple images into one that preserves the interesting detail of each [65]. The wavelet transform affords a convenient way to fuse images. One simply takes, at each coefficient position, the coefficient value having maximum absolute amplitude and then reconstructs an image from all such maximum-amplitude coefficients. If the basis functions match the interesting components of the image, then the fused image will contain the interesting components collected up from all of the input images. The images can be combined in the transform domain by taking the maximum-amplitude coefficient at each coordinate. An inverse wavelet transform of the resulting coefficients then reconstructs the fused image. We found that deblurring prior to wavelet fusion significantly improves the measured sharpness of the processed images. An example of wavelet image fusion using transmitted light and fluorescence images is shown in Fig. 19. Optical section deblurring followed by image fusion produced an image in which all of the dots are visible for the fluorescence images. We use these techniques to improve the information content of images from thick samples. Specifically, this technique improves the dot information in acquired FISH images because it incorporates data from focal planes above and below.

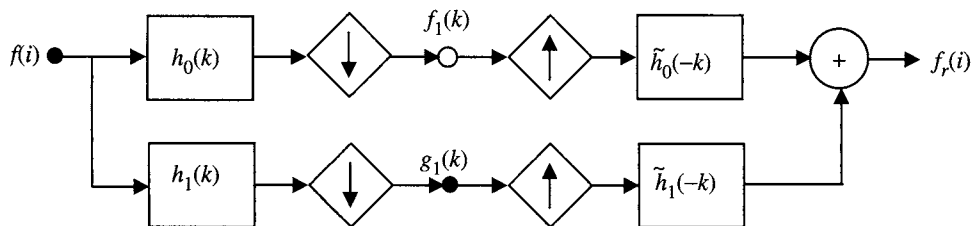


FIGURE 18 Mallat’s (1-D) DWT Algorithm. The left half shows one step of decomposition, while the right half shows one step of reconstruction. The down and up arrows indicate downsampling and upsampling by a factor of two, respectively. For an orthonormal transform, the two filters on the right are the same as the two on the left. Further steps of decomposition and reconstruction are introduced at the open circle.

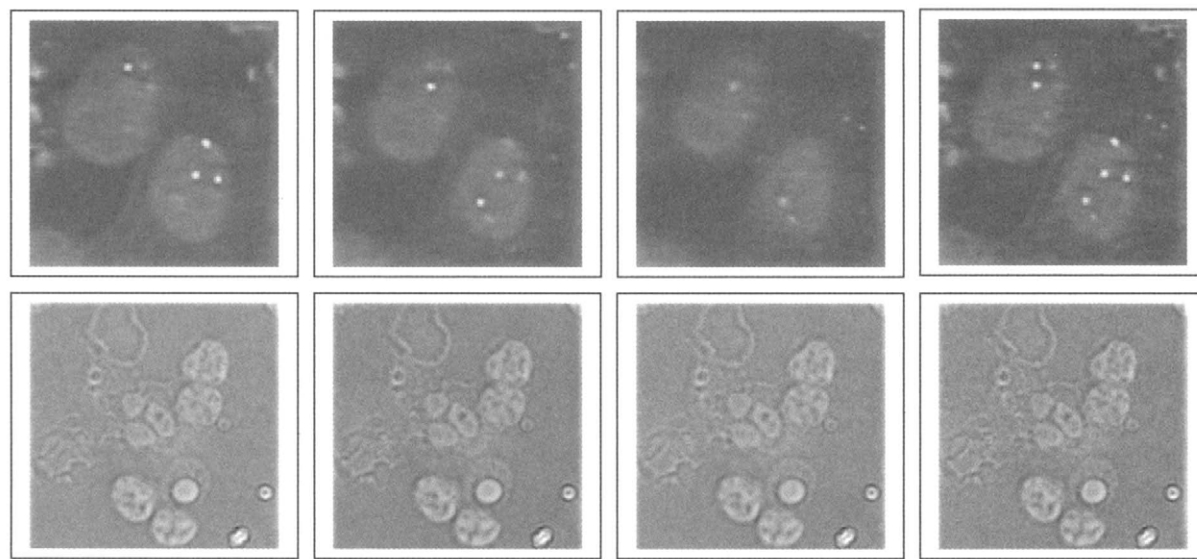


FIGURE 19 Image Fusion using transmitted light and fluorescence images. The top row shows FISH-labeled lymphocytes. The left three images are from a deblurred optical section stack taken one micron apart. The right image is the fusion of the three using the Biorthogonal 2, 2 wavelet transform. Notice that the fused image has all of the dots in focus. The bottom rows demonstrate a similar effect in transmitted light images. The deblurring process, followed by image fusion, enhances image detail (see color insert).

6.6 Commercially Available Systems

Computer-assisted microscopy systems can vary in price, sensitivity, and capability. The selection of a system depends upon the experimental applications for which it will be used. Typically, the selection is based on requirements for image resolution, sensitivity, light conditions, image acquisition time, image storage requirements, and most important, the postacquisition image processing and analysis required. Other considerations are the technical demands of assembling the component hardware and configuring software. Computerized imaging systems can be assembled from component parts or obtained from a supplier as a fully integrated system. Several companies offer fully integrated computerized microscopy system, and/or provide customized solutions for specialized systems.

A brief listing of some of the commercially available systems is provided here. Applied Precision Inc., (Issaquah, WA), provides a computerized imaging instrument, the Delta-VisionTM Restoration Microscopy System for applications such as 3D time-course studies with live cell material. Applied Precision also offers the softWoRxTM Imaging Workstation for postacquisition image processing such as deconvolution, 3D segmentation, and rendering. Universal Imaging Corporation (West Chester, PA) provides software, including the Meta-MorphTM, MetaViewTM, and MetaFluorTM systems, that can be customized for computerized microscopy applications in transmitted light, time-lapse studies, and fluorescence microscopy. VayTek Inc., (Fairfield, Iowa) provides an integrated microscopy imaging system, the ProteusTM system that can be custom configured to any microscopy system. VayTek's

proprietary software for deconvolution and 3D reconstruction, including MicroTomeTM, VoxBlastTM, HazeBusterTM, VtraceTM, and Volume-ScanTM, can also be custom configured for most current microscopy systems. ChromaVision Medical Systems Inc., (San Juan, CA), provides an Automated Cellular Imaging System (ACIS) that allows cell detection based on color-, size-, and shape-based morphometric features. Meta-Systems GmbH, (Altlussheim, Germany) provides a computerized microscopy system based on Zeiss optics for scanning and imaging pathology slides, cytogenetic slides for FISH, MFISH, and metaphase detection, oncology slides and for rare cell detection, primarily from blood, bone marrow, or tissue section samples. Applied Imaging Corporation (Santa Clara, CA) provides fully automated scanning and image analysis systems. Their MDSTM system provides automated slide scanning using bright-field or fluorescent illumination to allow standard karyotyping, FISH, comparative genomic hybridization, and rare cell detection. Applied Imaging also has the OncopathTM and Ariol SI-50TM image analysis systems for oncology and clinical pathology applications.

The field of automated imaging is also of great interest to pharmaceutical and biotechnology companies. Many are now developing high-throughput and high-content screening platforms for automated analysis of intracellular localization and dynamics of proteins and visualizing the effects of a drug on living cells more quickly. High-content imaging systems for cell-based assays have proliferated in the past year; examples include Cellomic's ArrayScan system and KineticScan workstation (Cellomics, Inc., Pittsburgh, PA); Amersham's INCell Analyzer 1000 and 3000 (Amersham Biosciences Corp., Piscataway, NJ); Acumen Bioscience's Explorer

system (Melbourn, United Kingdom); CompuCyte's iCyte imaging cytometer and LSC laser scanning cytometer (CompuCyte Corporation, Cambridge, MA); Atto Bioscience's Pathway HT kinetic cell imaging system (Atto Bioscience Inc., Rockville, MD); Universal Imaging's Discovery-1 system (Universal Imaging Corporation, Downingtown, PA); and Q3DM's EIDAQ 100 High-Throughput Microscopy (HTM) system (Q3DM, San Diego, CA).

7 Conclusions

The rapid development of microscopy techniques over the few decades has been accompanied by similar advances in the development of new fluorescent probes, and improvements in automated microscope systems and software. Advanced applications such as deconvolution, FRET, and ion ratio imaging require sophisticated routines for controlling automated microscopes and peripheral devices such as filter wheels, shutters, automated stages, and cameras. Computer-assisted microscopy provides the ability to enhance the speed of microscope data acquisition and data analysis, thus relieving humans of tedious tasks. Not only the cost efficiency is improved due to the corresponding reduction in labor costs and space, but also errors associated with operator bias are eliminated. Researchers are relieved not only from tedious manual tasks, but may also quickly examine thousands of cells, plates, and slides, as well as precisely determine some informative activity against a cell, and collect and mine massive amounts of data. The process is also repeatable and reproducible with a high degree of precision.

We have described a specific configuration of a computerized fluorescence microscope with applications in clinical cytogenetics. Fetal cell screening from maternal blood has the potential to revolutionize the future of prenatal genetic testing, making noninvasive testing available to all pregnant women. Its clinical realization will be practical only via an automated screening procedure, because of the rare number of fetal cells available. Specialized slides, based on the grid template such as the subtelomeric FISH assay, require automated scanning methods to increase accuracy and efficiency of the screening protocol. Similarly, automated techniques are necessary to allow the quantitative analysis for the measurement of the separation distance for detection of duplicated genes. Thick-specimen imaging using deblurring methods allows the detection of cell structures that are distributed throughout the volume of the entire cell. Thus, there are sound reasons for pursuing the goal of automation in medical cytogenetics. Not only does automation increase laboratory throughput, it also decreases laboratories' costs for performing tests. And, as tests become more objective, the liability of laboratories decreases. The market for

comprehensive automated tests is vast in terms of size (whether measured in test volume or dollars) and potential impact on people's lives.

The effective commercial use of computer-assisted microscopy and quantitative image analysis requires the careful integration of automated microscopy, high-quality image acquisition, and powerful analytical algorithms that can rationally detect, count, and quantify areas of interest. Typically, the systems should provide walk-away scanning operation with automated slide loaders that can queue several (50–200) slides. Additionally, the automated microscopy systems should have the capability to integrate with viewing stations to create a network for reviewing images, analyzing data, and generating reports. There has been an increase in the commercialization of computerized microscopy and high-content imaging systems, over that past 5 years. Clearly, future developments in this field will be of great interest to biotechnology. All signs indicate that superior optical instrumentation and software for cell research are on the development horizon.

Acknowledgments

We would like to thank Vibeech Bose at Advanced Digital Imaging Research, LLC, and Hyojoon Choi and Mehul Sampat at The University of Texas at Austin, for their assistance with the development and testing of ADIR's computerized microscopy system. The development of the automated microscopy system was partially supported by National Institutes of Health SBIR grant nos. HD34719-02, HD38150-02, and GM60894-01.

References

- [1] M. Bravo-Zanoguera, B. Massenbach, A. Kellner, et al., "High-performance autofocus circuit for biologic microscopy," *Rev. Sci. Instrum.* 69, 3966–3977 (1998).
- [2] J. C. Oosterwijk, C. F. Knepfle, W. E. Mesker, et al., "Strategies for rare-event detection: an approach for automated fetal cell detection in maternal blood," *Am. J. Hum. Genet.* 63, 1783–1792 (1998).
- [3] L. A. Kamenstsky, L. D. Kamenstsky, J. A. Fletcher, et al., "Methods for automatic multiparameter analysis of fluorescence *in situ* hybridized specimens with a laser scanning cytometer," *Cytometry*, 27, 117–125 (1997).
- [4] H. Netten, I. T. Young, L. J. van Vliet, et al., "FISH and chips: automation of fluorescent dot counting in interphase cell nuclei," *Cytometry*, 28, 1–10 (1997).
- [5] I. Raykin and V. Temov, "Automated microscopy system for detection and genetic characterization of fetal nucleated red blood cells on slides," *Proc. Opt. Invest. Cells In Vitro In Vivo*, 3260, 180–191 (1998).
- [6] D. J. Stephens and V. J. Allan, "Light microscopy techniques for live cell imaging," *Science*, 300, 82–86 (2003).

- [7] T. Lehmann, J. Brendo, V. Metzler, et al., "Computer assisted quantification of axo-somatic buttons at the cell membrane of motoneurons," *IEEE Trans. Biomed. Eng.* 48, 706–717 (2001).
- [8] J. Lu, D. M. Healy, and J. B. Weaver, "Contrast enhancement of medical images using multiscale edge representation," *Opt. Engin.* 33, 2151–2161 (1994).
- [9] J. S. Ploem, A. M. van Driel-Kulker, L. Goyarts-Veldstra, et al., "Image analysis combined with quantitative cytochemistry," *Histochemistry*, 84, 549–555 (1986).
- [10] E. M. Slayter and H. S. Slayter, *Light and Electron Microscopy* (Cambridge University Press, 1992).
- [11] I. T. Young, "Quantitative microscopy," *IEEE Engin. Med. Biology*, 15, 59–66 (1996).
- [12] J. D. Cortese, "Microscopy paraphernalia: accessories and peripherals boost performance," *Scientist*, 14, 26 (2000).
- [13] E. T. Johnson and L. J. Goforth, "Metaphase spread detection and focus using closed circuit television," *J. Histochem. Cytochem.* 22, 536–545 (1974).
- [14] B. Dew, T. King, and D. Mighdoll, "An automatic microscope system for differential leucocyte counting," *J. Histochem. Cytochem.* 22, 685–696 (1974).
- [15] H. Harms and H. M. Aus, "Comparison of digital focus criteria for a TV microscope system," *Cytometry*, 5, 236–243 (1984).
- [16] F. C. Groen, I. T. Young and G. Lighthart, "A comparison of different focus functions for use in autofocus algorithms," *Cytometry*, 6, 81–91 (1985).
- [17] F. R. Boddeke, L. J. van Vliet, H. Netten, et al., "Autofocusing in microscopy based on the OTF and sampling," *Bioimaging*, 2, 193–203 (1994).
- [18] L. Firestone, K. Cook, K. Culp, et al., "Comparison of autofocus methods for automated microscopy," *Cytometry*, 12, 195–206 (1991).
- [19] D. Vollath, "Automatic focusing by correlative methods," *J. Microsc.* 147, 279–288 (1987).
- [20] D. Vollath, "The influence of scene parameters and of noise on the behavior of automatic focusing algorithms," *J. Microsc.* 152, 133–146 (1988).
- [21] J. F. Brenner, B. S. Dew, J. B. Horton, et al., "An automated microscope for cytologic research," *J. Histochem. Cytochem.* 24, 100–111 (1976).
- [22] A. Erteza, "Depth of convergence of a sharpness index autofocus system," *Appl. Opt.* 15, 877–881 (1976).
- [23] A. Erteza, "Sharpness index and its application to focus control," *Appl. Opt.* 16, 2273–2278 (1977).
- [24] R. A. Muller and A. Buffington, "Real time correction of atmospherically degraded telescope images through image sharpening," *J. Opt. Soc. Am.* 64, 1200–1210 (1974).
- [25] J. H. Price and D. A. Gough, "Comparison of phase-contrast and fluorescence digital autofocus for scanning microscopy," *Cytometry*, 16, 283–297 (1994).
- [26] J. M. Geusebroek, F. Cornelissen, A. W. Smeulders, et al., "Robust autofocusing in microscopy," *Cytometry*, 39, 1–9 (2000).
- [27] A. Santos, C. Ortiz de Solorzano, J. J. Vaquero, et al., "Evaluation of autofocus functions in molecular cytogenetic analysis," *J. Microsc.* 188, 264–72 (1997).
- [28] J. C. Russ, *The Image Processing Handbook* (CRC Press, Boca Raton, FL, 1994).
- [29] K. R. Castleman, T. P. Riopka and Q. Wu, "FISH image analysis," *IEEE Engin. Med. Biol.* 15, 67–75 (1996).
- [30] E. R. Dougherty and J. Astola, *An Introduction to Nonlinear Image Processing* (SPIE, Bellingham, WA, 1994).
- [31] J. Serra, *Image Analysis and Mathematic Morphology* (Academic Press, London, 1982).
- [32] K. R. Castleman, "Digital image color compensation with unequal integration periods," *Bioimaging*, 2, 160–162 (1994).
- [33] W. E. Higgins, W. J. T. Spyra, E. L. Ritman, et al., "Automatic extraction of the arterial tree from 3D angiograms," *IEEE Conf. Engin. Med. Biol.* 2, 563–564 (1989).
- [34] N. Niki, Y. Kawata, H. Satoh, et al., "3D imaging of blood vessels using x-ray rotational angiographic system," *IEEE Med. Imaging Conf.* 3, 1873–1877 (1993).
- [35] C. Molina, G. Prause, P. Radeva, et al., "3D catheter path reconstruction from biplane angiograms," *SPIE*, 3338, 504–512 (1998).
- [36] A. Klein, T. K. Egglan, J. S. Pollak, et al., "Identifying vascular features with orientation specific filters and b-spline snakes," *IEEE Comput. Cardiol.* 113–116 (1994).
- [37] A. K. Klein, F. Lee and A. A. Amini, "Quantitative coronary angiography with deformable spline models," *IEEE Trans. Med. Image*, 16, 468–482 (1997).
- [38] D. Guo and P. Richardson, "Automatic vessel extraction from angiogram images," *IEEE Comput. Cardiol.* 25, 441–444 (1998).
- [39] Y. Sato, S. Nakajima, N. Shiraga, et al., "3D multi-scale line filter for segmentation and visualization of curvilinear structures in medical images," *IEEE Med. Image Anal.* 2, 143–168 (1998).
- [40] P. E. Summers and A. H. Bhalerao, "Derivation of pressure gradients from magnetic resonance angiography using multi-resolution segmentation," *Proc. Int. Conf. Image Process. Appl.* 404–408 (1995).
- [41] T. McInerney and D. Terzopoulos, "Deformable models in medical image analysis: a survey," *IEEE Med. Image. Anal.* 1, 91–108 (1996).
- [42] F. Quek and C. Kirbas, "Vessel extraction in medical images by wave propagation and traceback," *IEEE Trans. Med. Image*, 20, 117–131 (2001).
- [43] C. Smets, G. Verbeeck, P. Suetens, et al., "A knowledge-based system for the delineation of blood vessels on subtraction angiograms," *Pattern Rec. Lett.* 8, 113–121 (1988).
- [44] R. Nekovei and Y. Sun, "Back-propagation network and its configuration for blood vessel detection in angiograms," *IEEE Trans. Neural Nets.* 6, 64–72, (1995).
- [45] K. R. Castleman, *Digital Image Processing* (Prentice Hall, NJ, 1996).
- [46] T. Ridler and S. Calvard, "Picture thresholding using an iterative selection method," *IEEE Trans. Syst. Man. Cybernet.* 8, 629–632 (1978).
- [47] W. Tsai, "Moment-preserving thresholding," *Comput. Vis. Graph. Image Process.* 29, 377–393 (1985).
- [48] N. Otsu, "A threshold selection method from gray-level histograms," *IEEE Trans. Syst. Man. Cybernet.* 9, 62–66 (1979).
- [49] J. Kapur, P. Sahoo and A. Wong, "A new method for gray-level picture thresholding using the entropy of the histogram," *Comput. Vis. Graph. Image Process.* 29, 273–285 (1985).

- [50] H. Firth, P. A. Boyd, P. Chamberlain, et al., "Severe limb abnormalities after chorionic villus sampling at 56 to 66 days," *Lancet*, 1, 762–763 (1991).
- [51] D. Ganshirt-Ahlert, M. Burschyk, H. P. Garritsen, et al., "Magnetic cell sorting and the transferrin receptor as potential means of prenatal diagnosis from maternal blood," *Am. J. Obstet. Gynecol.* 166, 1350–1355 (1992).
- [52] D. W. Bianchi, G. K. Zickwolf, M. C. Yih, et al., "Erythroid-specific antibodies enhance detection of fetal nucleated erythrocytes in maternal blood," *Prenat. Diagn.* 13, 293–300 (1993).
- [53] S. Elias, J. Price, M. Dockter, et al., "First trimester prenatal diagnosis of trisomy 21 in fetal cells from maternal blood," *Lancet*, 340, 1033 (1992).
- [54] F. A. Merchant, S. J. Aggarwal, K. R. Diller, et al., "Three-dimensional distribution of damaged cells in cryopreserved pancreatic islets as determined by laser scanning confocal microscopy," *J. Microscopy*, 169, 329–338 (1993).
- [55] K. R. Castleman and B. S. White, "Dot-count proportion estimation in FISH specimens," *Bioimaging*, 3, 88–93 (1995).
- [56] F. A. Merchant and K. R. Castleman, "Strategies for automated fetal cell screening," *Hum Reprod. Update*, 8, 509–521, (2002).
- [57] S. J. Knight and J. Flint, "Perfect endings: a review of subtelomeric probes and their use in clinical diagnosis," *J. Med. Genet.* 37, 401–409 (2000).
- [58] X. Hu, A. M. Burghes, P. N. Ray, et al., "Partial gene duplication in Duchenne and Becker muscular dystrophies," *J. Med. Genet.* 25, 369–376 (1988).
- [59] K. S. Chen, P. Manian, T. Koeuth, et al., "Homologous recombination of a flanking repeat gene cluster is a mechanism for a common contiguous gene deletion syndrome," *Nature Genet.* 17, 154–163 (1997).
- [60] L. Potocki, K. Chen, S. Park, et al., "Molecular mechanism for duplication 17p11.2: the homologous recombination reciprocal of the Smith-Magenis microdeletion," *Nature Genet.* 24, 84–87 (2000).
- [61] W. H. Press, W. T. Flannery, S. A. Teukolsky, et al., *Numerical Recipes in C* (Cambridge University Press, New York, 1992).
- [62] M. Weinstein and K. R. Castleman, "Reconstructing 3D specimens from 2D section images," *Proc. SPIE*, 26, 131–138 (1971).
- [63] S. Mallat, "A theory for multiresolution signal decomposition: the wavelength representation," *IEEE Trans. Patt. Anal. Mach. Intell.* 11, 674–693 (1989).
- [64] I. Daubechies, "Orthonormal bases of compactly supported wavelets," *Commun. Pure Appl. Math.* 41, 909–996 (1988).
- [65] J. Aggarwal, *Multisensor Fusion for Computer Vision* (Springer-Verlag, New York, 1993).

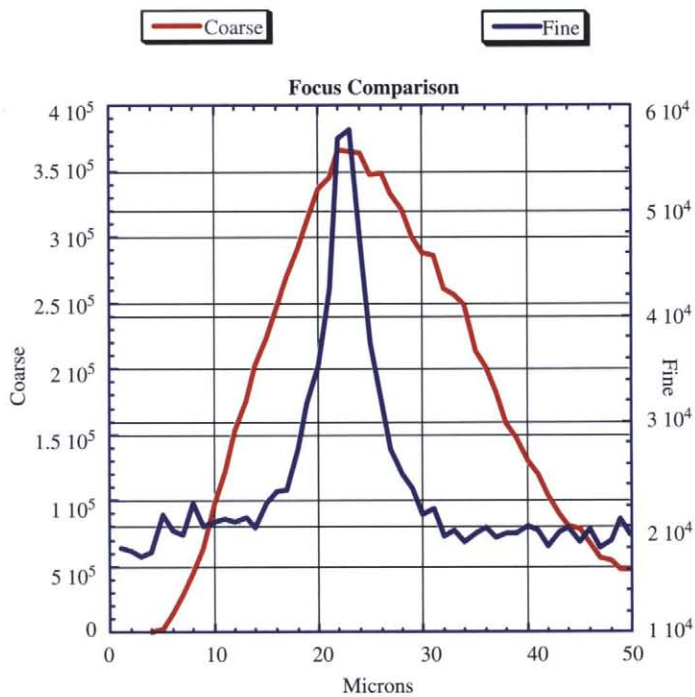


FIGURE 10.10.2 Two-phase approach to autofocusing, using a coarse focus and a separate fine focus function.

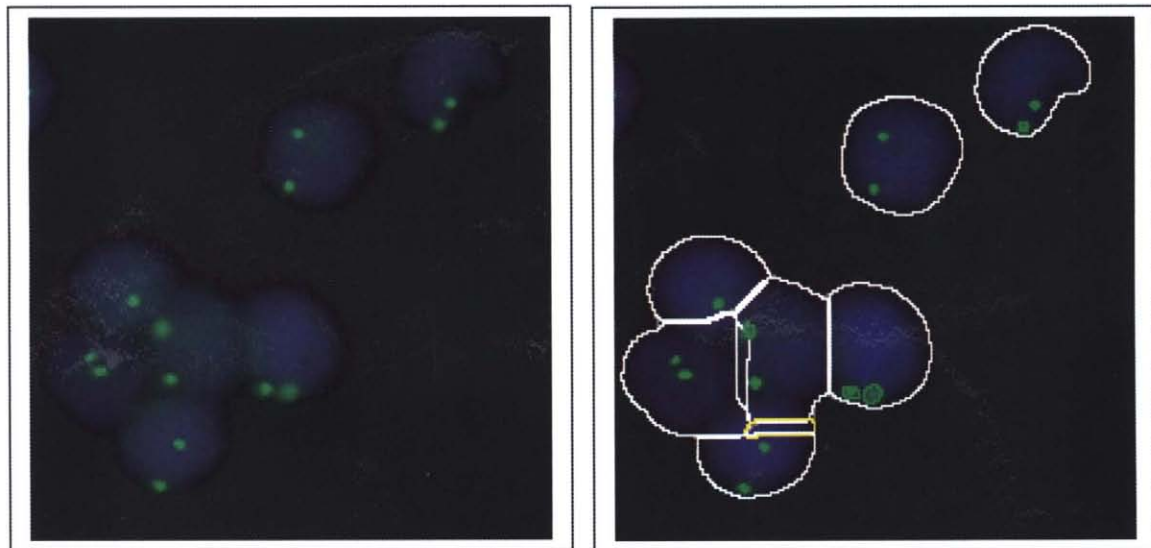


FIGURE 10.10.4 Fluorescence image of 7 female (XX) cells. Adult female blood was processed via FISH. Cells are counterstained blue (DAPI); X chromosomes are labeled in green (FITC). Results of automated image analysis. As illustrated in the right panel the software accurately detects single cells, separates touching cells, and detects the green dots in individual cells.

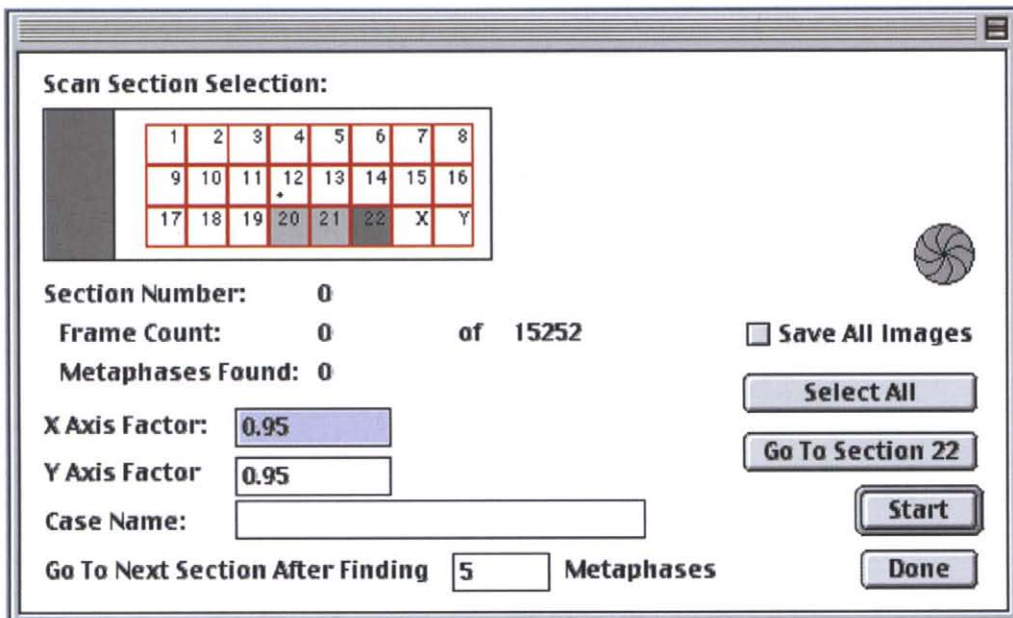


FIGURE 10.10.6 User interface for automated scanning of the Cytocell Multiprobe® template microscope slide. The user can select a region to scan at the click of a mouse button (Ex: regions 20, 21 and 22 were selected above). Either the entire selected region can be scanned, or the user can define the number of metaphases per region (Ex: 5 Metaphases, as shown above). Scanning then continues with the next selected region. The X-axis and Y-axis factors adjust the scanning step-size in X and Y, and may be used to capture overlapping regions to avoid the loss of cells that fall between adjacent image frames.



Figure 10.10.8 The output of the metaphase finding algorithm. The isolated objects are labelled aa-az, ba-bz, and ca (total 53 objects), and then classified using the parameters described in Fig. 7. The objects in green were classified as objects of a cluster, while red objects are rejected. A cluster of objects outlined by a green box is identified as a metaphase, while cluster objects outlined by a red box are rejected.

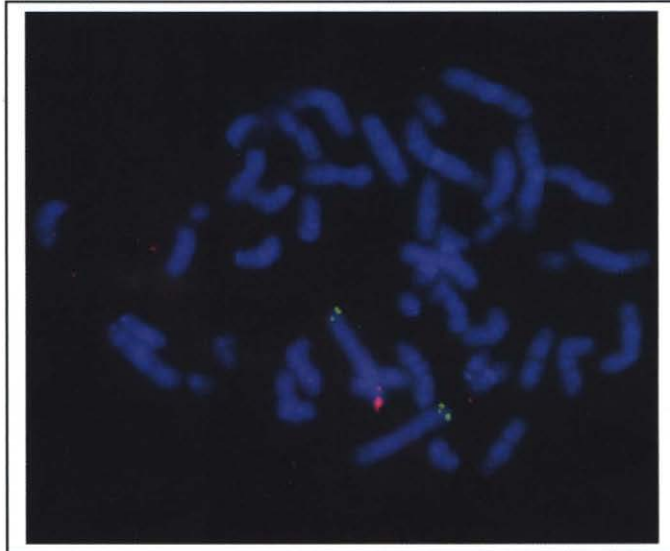


FIGURE 10.10.9 FISH was performed using subtelomeric DNA probes for chromosome 2. The q-arms are labeled red (Texas Red) and the p-arms are labeled green (FITC). This specimen is deleted for distal 2q (monosomic). Subtelomeric FISH was performed using the Chromoprobe Multiprobe[®] T System from Cytocell Ltd. Imaging was performed using the ADIR computerized microscopy system.

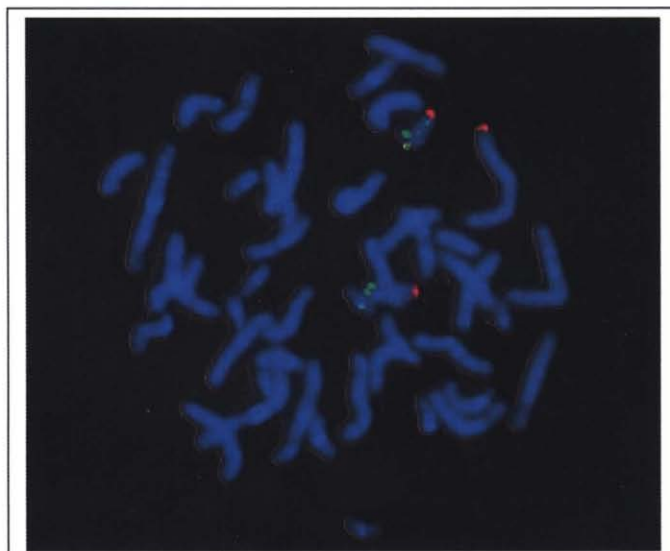


FIGURE 10.10.10 FISH was performed using subtelomeric DNA probes for chromosome 17. The q arms are labeled red (Texas Red) and the p arms are labeled green (FITC). The specimen is trisomic for distal 17q, and carries a cryptic translocation (derivative 2). Subtelomeric FISH was performed using the Chromoprobe Multiprobe[®] T System from Cytocell Ltd. Imaging was performed using the ADIR computerized microscopy system.